8-2013

Deformation Behavior of Bulk Metallic Glasses and High Entropy Alloys by Nanoindentation

Yuting Li
yli82@utk.edu

To the Graduate Council:

I am submitting herewith a thesis written by Yuting Li entitled "Deformation Behavior of Bulk Metallic Glasses and High Entropy Alloys by Nanoindentation." I have examined the final electronic copy of this thesis for form and content and recommend that it be accepted in partial fulfillment of the requirements for the degree of Master of Science, with a major in Materials Science and Engineering.

Peter K. Liaw, Major Professor

We have read this thesis and recommend its acceptance:

Thomas T. Meek, Mariya Zhuravleva

Accepted for the Council:
Dixie L. Thompson

Vice Provost and Dean of the Graduate School

(Original signatures are on file with official student records.)

8-2013

Deformation Behavior of Bulk Metallic Glasses and High Entropy Alloys by Nanoindentation

Yuting Li
yli82@utk.edu

To the Graduate Council:

I am submitting herewith a thesis written by Yuting Li entitled "Deformation Behavior of Bulk Metallic Glasses and High Entropy Alloys by Nanoindentation." I have examined the final electronic copy of this thesis for form and content and recommend that it be accepted in partial fulfillment of the requirements for the degree of Master of Science, with a major in Materials Science and Engineering.

Peter K. Liaw, Major Professor

We have read this thesis and recommend its acceptance:

Thomas T. Meek, Mariya Zhuravleva

Accepted for the Council:
Carolyn R. Hodges

Vice Provost and Dean of the Graduate School

(Original signatures are on file with official student records.)

Deformation Behavior of Bulk Metallic Glasses and High Entropy Alloys by Nanoindentation

A Thesis Presented for the

Master of Science

Degree

The University of Tennessee, Knoxville

Yuting Li

August 2013

Dedication

This dissertation is dedicated to my parents, Dechang Li and Yimei Zhi, my wife, Zhibo Tan, and my son, Eric Minghao Li, and the rest of my families and my friends, for their love, encouragement, and support.

Acknowledgement

First and foremost, I would like to express my deep gratefulness to my advisor, Dr. Peter K. Liaw, for his guidance and the endless support during my master degree study at The University of Tennessee in Knoxville. His patience, motivation, enthusiasm will accompany with me on my work and study in the future.

I also specially like to thank Dr. Thomas T. Meek and Dr. Mariya Zhuravleva for serving on my thesis committee. I am going to give my special thanks to Prof. Fuqian Yang and Dr. Guangfeng Zhao from The University of Kentucky for their kind help on the nanoindentation tests. I greatly appreciate the guidance on irradiation simulation from Prof. Yanwen Zhang and Prof. William J. Weber. I would like to thank Dr. Gongyao Wang and Mr. Douglas E. Fielden at The University of Tennessee for their generous help and encouragement with my research and dissertation. I would also like to express my sincere appreciation to all the members of Dr. Liaw's research group, Zhiqian Sun, Xie Xie, Zhinan An, Zhi Tang, Haoling Jia, Bilin Chen, ***et al.*** and thanks for their help and friendship. Special gratitude goes to my best friends during my study at The University of Tennessee, Mengkun Tian, Chao Zhu, Dong Wu, Qing Liu, Fang Meng, and Shaofang Fu, whose friendship is a big fortune in my life.

During the period of my master degree study, many people helped me on many aspects that are indispensable. Thanks to Dr. Joseph E. Spruiell for his kind teaching and operation of the X-ray technique. I am also thankful to Dr. John Dunlap and Gregory Jones for their kind instruction and the operation of a scanning electron microscopy (SEM).

Lastly and most importantly, I would like to dedicate my thesis to my parents, Dechang Li and Yimei Zhi, my wife, Zhibo Tan, and my son, Eric Minghao Li, for their love, encouragement, and support in all my pursuits.

Abstract

Nanoindentation has become a powerful tool in the measurement of the mechanical properties of diverse materials, such as metallic materials, polymer materials, and even biomaterials.

In this thesis, three types of Zr-based bulk metallic glasses (BMGs) were investigated by nanoindentation. Our work focuses on the characterization of the hardness, the reduced modulus, and the deformation behavior under different indentation conditions. The study of the hardness and the reduced modulus is to access the effect of the indentation load on deformation behavior and to determine the inhomogeneous deformation. The morphological profiles of the residual indentation on the surface of the specimen after an indentation were observed by the atomic force microscope (AFM). Differential scanning calorimetry (DSC) measurements were performed to determine characteristic thermal properties, the glass transition temperature (T_g), and the crystallization temperature (T_x).

The serrated-flow behavior (or pop-in behavior) was investigated at different loading rates. It is concluded that the pop-in size gradually increases with the decrease in the loading rate and the increase of the indentation depth. And the research of the indentation tests on the several metallic glasses at different indentation rates indicates that a much higher critical strain rate will lead to the disappearance of flow serrations.

Another type of material of a high-entropy alloy (HEA) was also investigated in this thesis. The hardness, reduced modulus, and deformation behavior were investigated by the indentation tests. Compared to Zr-based BMGs, this type of HEA

has lower hardness and higher reduced modulus. Creep behavior was observed in the indentation tests. However, serrated flow behavior disappears. The microstructure of this HEA was investigated by the X-ray diffraction (XRD), atomic force microscopy (AFM), scanning electron microscopy (SEM), and energy-dispersive spectroscopy (EDS). For the advanced research, the simulation of ion-implantation of HEAs was preformed, because the advanced reactor is one of the important potential applications of HEAs and advanced nuclear-energy systems, which will require materials that can withstand extreme reactor environments of high-temperature and high-doses radiation.

Table of Contents

List of Tables

List of Figures

Chapter 1 Literature Review

1.1 Introduction

For more than a century, the materials science researchers have recognized that mechanical properties are the determinant factor in surface contacts between materials. In order to measure such mechanical properties from a contact of known geometry, researchers have been developing many different indentation and impression tests. Due to the development of new sensors and actuators, the instrumented indentations can be routinely performed on submicron scales. Thus, the nanoindentation was developed for mechanical-property measurements at surfaces. It is well known that the metals are the workhorse material of the modern society, owing to their excellent formability, toughness, and strength. Bulk metallic glasses (BMGs) and high entropy alloys (HEAs) are the alloys developed in recent years and have novel properties, such as high strength. Thus, nanoindentation is a very good instrument to research the fundamental deformation mechanisms of these materials [1, 2]. In our work, we will focus on the characterization of the hardness, reduced modulus, serrated flow, and many other properties of BMGs and HEAs by nanoindentation.

1.2 Nanoindentation

The nanoindentation technique, developed in the mid-1970s [3, 4], has been widely used to test mechanical properties of materials in the last decades, and it is commonly applied in the small volume of samples at small scales [1, 2]. Traditionally,

the indentation experiment is only used to test the hardness of a material, until Ternovskii *et al.* [4] derives the reduced modulus of interest using the measured load-displacement data by introducing the stiffness equation. The stiffness equation introduced by Ternovskii *et al.* is as follows

$$\frac{dP}{dh} = \frac{2}{\sqrt{p}} E_r \sqrt{A} \tag{1}$$

where dP/dh is the slope of the load-displacement curve, E_r is the reduced modulus of a material, and A is the projected contact area of the indent. Oliver and Pharr [1] re-introduce the stiffness equation and claim that this equation can be used in all axisymmetric indenters with any infinitely smooth profile. They proposed this technical approach, which received the wide acceptance by the community, and make the nanoindentation as a technique very popular to extract elastic material properties.

This method of nanoindentation is derived from traditional indentation tests. However, the size of manufactured tips was reduced, and the accuracy and resolution of depth were improved due to the technological developments [5]. The hardness value and elastic modulus are the primary properties, which were measured by means of nanoindentation, and it measures the load-displacement response by the high-resolution equipment. Moreover, with the increased interest in small volumes of thin films and specimens and the modern applications, nanoindentations become more and more popular and have some new innovations, such as the atomic force microscopy (AFM) [6, 7, 8] or in-suit transmission electron microscopy (TEM) [9,10,11]. Nanoindentation has also been used to research the rate-dependent

processes, such as mechanical properties of creep [12]. Furthermore, the development of the high-temperature stage helps the research on the temperature dependence of mechanical properties. The nanoindentation technique has some relative advantages in mechanical testing in the sub-micron range, when compared to other testing methods, such as the simple setup and specimen preparation, leaving a small imprint and commonly perceived as relatively nondestructive [13].

Several analytical approaches have been developed for measuring mechanical properties, such as hardness, elastic modulus, and yield stress from the indentation load-displacement data of a bulk material. The typical procedure of the nanoindentation experiment is to use a specially-designed tip penetrating into a specimen, records the load and the corresponding displacement, and then use the load and displacement to calculate the hardness and elastic modulus. To date, many kinds of indentation tips are designed with the development of the indentation technique, and the different kinds of indentation tips and their characterization are summarized in Figure 1. In our experiments, we simply use the diamond Berkovich tip, which is also used most widely. The Berkovich tip is a three-sided pyramid, which is geometrically self-similar and the centerline-to-face angle, α , is 65.35°, as shown in Figure 2 [14].

The most common method was developed to measure the hardness and the reduced modulus of a material from the load-displacement data obtained with the Berkovich indenter, which was proposed by Oliver and Pharr in 1992 [1]. Figure 3 is a schematic profile of the indentation process for the Berkovich indenter. When the indenter is penetrating into the specimen, both elastic and plastic deformations on the

material's surface occur, which produces an impression in the specimen that has the same geometric shape of the indenter, and generates a contact depth referred to as h_c.

The typical loading and unloading procedure consists of five steps:

(1) Increasing the load linearly to a determined maximum value (P_{max}) at a constant loading rate;

(2) Holding the load of P_{max} constant for the different hold time, t_{hold};

(3) Decreasing linearly the load to 10% of P_{max} with the same rate as the loading stage;

(4) Holding the load constant for a specified time to record the thermal drift of the instrument;

(5) Decreasing the load linearly to zero with the same loading rate as the loading stage.

The hardness and reduced modulus can be calculated by analyzing the load-displacement curve, as shown in Figure 4. In order to calculate the hardness of a material from the nanoindentation data, some important quantities must be recorded by the test system, such as maximum load (P_{max}), maximum depth (h_{max}), and the final depth of the residual hardness impression (h_f). The equation used to extract the hardness, H, is:

$$H = \frac{P_{\max}}{A} \tag{2}$$

where P_{max} is the peak load, and A is the project contact area at the peak load. For the unloading stiffness, S, is determined by curve-fitting the upper portion of the

unloading curve and measuring its slope at the peak load and the equation is:

$$S = \left[\frac{dP}{dh}\right]_{unloading} = \frac{2b}{\sqrt{p}} E_r \sqrt{A} \tag{3}$$

Here, $S = dP/dh$ is the experimentally-measured stiffness of the upper portion of the unloading data, and E_r is the reduced modulus. The widely-used relationship for the reduced modulus, E_r, which relates projected area, A, and contact stiffness, S. is given by

$$E_r = \frac{1}{b}\frac{\sqrt{p}}{2}\frac{S}{\sqrt{A}} \tag{4}$$

where β is a correction factor corresponding to the geometry of the indenter, with β = 1 for axisymmetric indenters and β = 1.03～1.05 for indenters with square or rectangular cross sections. The relationship between the elastic modulus of the specimen, E, and the measured reduced modulus, E_r, are given by the following equation as:

$$\frac{1}{E_r} = \frac{1-n_S^2}{E_S} + \frac{1-n_i^2}{E_i} \tag{5}$$

where n_i and E_i are the Poisson's ratio and elastic modulus for the indenter, and v_S and E_S are the same parameters for the specimen, respectively. For the diamond indenter, E_i equals to 1,141 GPa and n_i equals to 0.07 [15]. Hey *et al.* [16] point out that even if the material's Poisson ratio is roughly estimated around 0.25 ± 0.1, there still has more than 5% uncertainty in the calculated value of E for the materials.

1.3 Bulk Metallic Glass

Metallic glasses (that is, metallic amorphous glasses), first formatived by Duwez at Caltech, USA, in 1960 [17], are alloys without long-range periodicity or quasicrystalline common to conventional metals. They used the rapid quenching techniques to freeze the liquid structure at an extremely high rate of $10^6 K/s$ to avoid the crystallization. Following this discovery, the research on the metallic glasses was accelerated in the early 1970s because a melt spinning method was invented and developed [18]. This technique, which is a rapid cooling method, can quench liquid alloys through impinging a melt stream on a spinning copper wheel with 10 – 50 μm thick ribbons at cooling rates of $10^3 – 10^6$ *K/s*. At this stage, the formation of metallic glasses should require the high cooling rates, and this trend limit the amorphous alloys geometry and restrict the development of the bulk metallic glasses. Therefore, the most important thing is to develop new metallic glasses with lower critical cooling rates for keeping the amorphous structure. However, some noble-metal-based alloys, such as Pd-Cu-Si and Pd-Ni-P [19, 20, 21], were found to the few exceptions. Drehman *et al.* [20] claim that these alloys could fabricated with very low critical cooling rates of ~10 *K/s*, and the bulk size of these glassy samples could be ~10 *mm* in thickness. Although this is a big development of the research in the BMGs, these pioneering works did not make any real impact in the materials science community. The main reason is that the noble metals, such as palladium and platinum, are very expensive and cannot be used for a wide range of applications, even if these metals are very good for improving the glass-forming ability.

Inoue *et al.* [22] discovered the multicomponent glass formers in 1990s, and these new bulk glassy alloys have very low critical cooling rates for the bulk glass formation and exhibit the excellent glass-forming ability (GFA). So, the discovery of multicomponent glass formers could be considered the breakthrough in the BMG research, because some inefficiencies transition metals, not the expensive noble metals, can be used for essential constituent elements in these new BMG alloys. Peker *et al.* [23] at Caltech in 1993 reported that they successfully prepared an excellent multicomponent BMG and the composition is $Zr_{41.2}Ti_{13.8}Cu_{12.5}Ni_{10.0}Be_{22.5}$, in atomic percent (at. %). The most important thing is that this new kind of BMG alloys contains 22.5 at% beryllium, which is first used as the glass former. Beryllium is the smallest metallic atom in the world. Thus, it is not only used to fill empty space in the defective glass structure, but also employed to make the stabilization of the liquid and glass phases more efficient.

Due to the excellent high thermal stability and glass-forming ability, metallic alloys, which are usually referred to as BMGs, have been paid much scientific and engineering attentions from the early 1970s to 1990s. During this time, many kinds of BMGs, such as iron-, nickel-, titanium-, copper-, and based zirconium-based alloy systems [24], have been developed and an explosion of academic and industrial study has occurred owing to their various applications.

With the development of BMGs, both the glass-forming ability and the critical casting thicknesses are increased observably. Siegrist *et al.* [25] reviewed the progress history of the research of the BMG alloys and summarized the critical casting

thicknesses of these metallic glasses in a plot, which is reprinted in Figure 5. It is pointed out that, over last four decades, the critical casting thickness tends to increase by one order of magnitude approximately every 12 years and increased total by more than three orders of magnitudes [25]. So far, more than one thousand of different BMGs have now been reported. In these different BMGs systems, the PdCuNiP family has the highest glass-forming ability and a critical casting thickness of 72 *mm* was developed by Inoue group.

1.3.1 BMG formation

A growing number of BMGs have been successfully prepared and commercialized for many potential structural and functional applications because of their novel properties. Although the glass forming ability (GFA), an important terminology in studying the metallic-glasses formation, has been improved with the development of metallic glasses, the relative low GFA is still one of the largest stumbling blocks for their commercial use. Many indicators of the GFA have been proposed, nevertheless, no standard definition has been made by now. From the engineering aspect, the higher GFA of a metallic glass need the lower critical cooling rate (R_c) and the larger critical dimension or thickness. Owing to the fact that it is still difficult to measure the critical cooling rate precisely in the experiment, the reliable criteria of characterizing the GFA need to be designed.

The first used indicator for predicting the GFA, the reduced glass-transition temperature, T_{rg} , was reported by Turnbull [26, 27] in 1970s. $T_{rg} = T_g / T_l$ where T_g

is glass-transition temperature, and T_l is liquid temperature or $T_{rg} = T_g / T_m$ where Tm is melting temperature. It is reported that when the T_{rg} in the range of 0.66-0.69, the metallic glasses have the high GFA [28]. Figure 6 shows a good correlation between the criterion, T_{rg}, and GFA [29].

In 1980s, Inoue [24] report a new kind of GFA indicator, ΔT_{xg}, the supercooled liquid region. $\Delta T_{xg} = T_x - T_g$ where T_x is the crystallization temperature, and T_g is the glass-transition temperature. The parameter indicates that with the increase of the accessible supercooled liquid region, there was corresponding improvement in GFA [30].

Some researchers point out that the T_{rg} has a better correlation than ΔT_{xg} with GFA in most glass-forming systems [31, 32]. However, with the prepared and development of new metallic-glass compositions, both indicators of T_{rg} and ΔT_{xg} show unreliable correlations with GFA, even presenting a contrasting trend in many BMGs systems [31]. For example, Shen *et al.* [33, 34] report that in some Pd- and Fe-based metallic-glasses compositions, T_{rg} is found to be unsatisfactory to predict GFA. Until recently, Lu *et al.* [35, 36] developed a new indicater, γ, which shows a reliable correlation to reflect the GFA of most metallic-glasses compositions and some oxide glasses. In Lu *et al.*[35, 36] theory, the average of the stability of the liquids in equilibrium and metastable states, $1/2(T_g + T_l)$, can be used to represent the liquid-phase stability if two liquids have different T_l and T_g, as shown in Figure 7. In general, a glass-forming liquid should have a relatively higher liquid phase stability if it has a smaller value of $1/2(T_g + T_l)$. If all liquids have the same liquid-phase

stability, the onset crystallization temperature, T_x, can assess the GFA alone, as shown in Figure 8, which schematically point out the function of T_x and GFA [36]. Thus, Lu *et al.* proposed a new indicator, γ, which is the normalized T_x and used as a gauge for GFA, expressed as follows [35, 37].

$$g \propto T_x \left[\frac{1}{2(T_g + T_l)} \right] \propto \frac{T_x}{T_g + T_l} \tag{6}$$

From this equation, it is clear that the higher onset crystallization temperature T_x, which represent greater resistance to crystallization, and the lower sum of T_g and T_l, which means lower stability in the metastable and equilibrium state, will result in higher γ, which gives good GFA. The correlation between the critical cooling rate, R_c and indicator, γ for typical bulk metallic glasses are shown in Figure 9 [36] and the correlation between the critical thickness, t_{max}, and indicator, γ, are shown in Figure 10 [36].

There are many other indicators proposed by the researchers. Fan *et al.* [38] proposed a dimensionless criterion, φ, ground on the theoretical calculations using the fragility concept and the nucleation theory, and the φ can be expressed by

$$f = T_{rg} \left(\frac{\Delta T_x}{T_g} \right)^a \tag{7}$$

where α is a constant. Based on the experimental data associated with the thermal analysis of BMG alloys, Chen *et al.* [39] proposed a new criterion, defined as $\delta = T_x/(T_l - T_g)$. The author claim that the δ criterion is distinctly better than other currently used criteria and it has a much better interrelationship with GFA than γ and

T_{rg}. Based on the nucleation and growth theory, Yuan *et al.* [40] proposed a dimensionless criterion, β, which can be expressed by

$$b = \frac{T_x \mathrm{g} T_g}{(T_l - T_x)^2} \tag{8}$$

It was also claimed that the new criterion, β, is better than other currently used criteria in statistical.

As mentioned above, GFA includes two important components: the stability of the liquid structure and the resistance to crystallization. Many criteria have been developed by the researchers. However, it is still a long way to develop proper indicators for GFA.

1.3.2 Mechanical properties and composites

Due to the absence of dislocations and crystalline lattice, we have the realization that the BMGs have a unique deformation mechanism, such as the high strength (> 2 GPa), high hardness (600 - 1,300 DPH), high fracture toughness (> 70 MPa·$m^{1/2}$), high elastic strain (~ 2% elastic strain), good castability and formability (> 1,000% elongation), superior aqueous corrosion resistance, good wear resistance, excellent soft magnetic properties (Fe-based BMGs) and other interesting optical and physical properties. Amiya and Inoue *et al.* prepared the (Fe, Co)-Cr-Mo-C-B-Tm glassy alloys in a cylindrical form with a diameter of 18 mm and they claim that this glassy alloys show an excellent GFA and high strength exceeding 4 GPa [41]. $Co_{43}Fe_{20}Ta_{5.5}B_{31.5}$ glassy alloy prepared by Inoue *et al.* [42] exhibiting ultrahigh

fracture strength over 5 GPa, high Young's modulus of 270 GPa, and it also have high specific strength and high specific Young's modulus. This glassy alloy also has excellent formability, which the large tensile elongation is 1,400%.

Mechanical properties of Zr-based BMGs with respect to yield (σ_y) and fracture strength (σ_f), vickers hardness as well as the Young's modulus (E) are given in Tables 1 and 2 [43].

1.3.3 Plastic deformation

Due to no grain boundaries or dislocations in BMGs, their deformation mechanisms are distinctly different from the conventional crystal materials and their plastic-deformation behavior cannot be explained by the traditional dislocation theory. Furthermore, the formation and rapid propagation of the localized shear bands be supposed to the reason of the deformation of BMGs at room temperature [44, 45].

To date, the inhomogeneous shear-band operation theory have a widely accepted [30, 46] and it can be used in many deformation process, such as nanoindentation [47, 48], bending [49], compression [46], and fatigue tests [50]. Figure 11(a) shows a typical nanoindentation impression induced by a Berkovich indent on the surface of a Pd-based metallic glass and Figure 11(b, c) present two load-displacemnet curve (***i.e*** the ***P-h*** curve) corresponding to the Pd-based metallic glass. It is well know that the rise of work hardening mechanisms which caused by the motion and mutual interaction of dislocations will make the crystalline metal's plastic flow stable,

however, no grain boundaries or dislocations in metallic glasses will lead to the unstable of the plastic deformation and shear-band emission [51, 52, 53, 54]. It has been reported that serrated flow is highly affected by the loading rate in BMGs under nanoindentation and uniaxial compression [55, 56, 57, 58, 59], as shown in Figure 12. A pattern of a typical loading rate dependence of the serrated flow in nanoindentation for BMGs show that the pop-in size gradually increases with the decrease in the loading rate, as shown in Figure 13 [58]. Although there have been many development on the understanding of the mechanical properties of BMGs from the literature above, there are still many problems needed to be explained by the researchers, such as source of the shear band on the BMGs.

1.4 High-entropy Alloys

An exciting new class of alloy, HEAs, has attracted increasing attention for their unusual structural properties in recent years [60, 61, 62]. They are typically defined as single-phase solid-solution alloys that consist of at least five principal metallic elements in equal or near-equal atomic percent (at. %), which is very different from the traditional alloy design, which is the major metallic element is selected based on a specific property requirement and other elements are added in with a small amounts to achieve different properties without sacrificing the primary one. Normally, the concentration of each element is between 5 and 35 at. %. Although consist of a large number of components, the HEA actually exhibit a surprising degree of mutual solubility in a single fcc phase or bcc phase [63]. Due to their high-temperature strengths, high hardness, corrosion resistance, wear

resistance and oxidation resistance [64], HEAs show great potential for engineering applications, making them favorable candidates for various elevated-temperature applications, such as advanced reactors, which require operating temperatures in excess of 750 ～ 850 °C for the next 80 years. Described thermodynamically using Boltzmann's Hypothesis, the configuration entropy, ΔS_{conf}, of random mixing of N elements is defined by the following equation:

$$\Delta S_{conf} = -R\sum_{1}^{n} x_i \ln x_i \tag{9}$$

where R is the gas constant, n is the number of elements, and x_i is the molar fraction. And the entropy of mixing of N elements approaches the maximum value, ΔS_m

$$\Delta S_m = R\ln N \tag{10}$$

So, ΔS_m increases rapidly with increasing the number of the alloying elements, when the elements are mixed at an equal or near-equal atomic percent.

One of the potential applications of HEAs, as an advanced reactor, in advanced nuclear-energy systems will require materials that can withstand extreme reactor environments of high-temperature and high-doses radiation. Knowledge of the radiation response in HEAs is, therefore, essential for their application in nuclear-energy systems. The irradiation studies will provide the critical understanding and data to validate computational predictions of radiation behavior in the HEA under high irradiation doses, such as 100 dpa, at temperatures to 700 °C. The experimental validation is essential to the assessment and development of the materials to be used in next-generation nuclear reactors. In the irradiation studies, the impacts of the

self-ion irradiation, such as Al, Co, and Ni, to simulate damage created by atomic collisions through primary recoils generated during fast neutron irradiation should be carried out. Very heavy ions, such as Au, will be used to study the HEAs' responses to high irradiation doses, which is an efficient way to provide the benchmark data in designing time-consuming self-ion irradiation experiments. In order to study the deformation behavior of the HEA before and after the irradiation, the experiment should be performed by nanoindentation.

1.5 Summary

Nanoindentation has become a powerful tool in the measurement of the mechanical properties of diverse materials, such as metallic materials, polymer materials, and even biomaterials. From the phase transformations in microscale of materials to the formation and motion of the defects, such as lattice dislocations or shear bands, the nanoindentation makes us have the considerable potential for understanding discrete atomic rearrangements under stress. From the literature review above, the researchers have been made many significant achievements on the studying of mechanical properties of BMGs in the past 40 years. The understanding of the deformation behavior of the BMGs also improved with the development of the nanoindentation technique. However, there are also several misunderstanding and debates on the mechanism for deformation behavior in BMGs. For example, the researchers still do not understand how the flow serration formed or where is the origin of a shear band even though it is widely accepted that the flow serration is

strongly associated with the shear-band emission.

The thesis focuses on the deformation behavior of the BMGs and HEAs under nanoindentation at the room temperature. The hardness and the reduced modulus also investigated in our indentation experiments. The different loading rate of the indentation will also be performed to research the serrated flow behavior.

Chapter 2 Experimental

2.1 Preparation of specimens

Zr-based BMGs specimens with the nominal composition of $Zr_{50}Cu_{40}Al_{10,}$ $Zr_{50}Cu_{30}Al_{10}Ni_{10}$, and $Zr_{65}Cu_{18}Ni_{7}Al_{10}$ atomic percent (at.%) were investigated in the present experiments. The amorphous alloy specimen were fabricated by the high-purity elements (Zr-99.5%; Cu-99.999%; Al-99.999%) and prepared by arc-melting master-alloy buttons in an argon environment. In order to obtain the low-oxygen concentration of the Zr-based BMGs, a special Zr-crystal rod, which oxygen content is less than 0.05 at.%, was used in the experiments [50]. At the temperature of 1,200 K, the melting was repeated at least five times to improve the chemical homogeneity of the alloys. The cast rod, 5 mm in diameter and 60 mm in length, was fabricated at a cooling rate of 100 K/s, using the tilt-casting method in an arc furnace via a pseudo-floating-melt state before casting to obtain a completely melted state [50]. Then the samples were machined into a cuboid with a length of 3 mm, width of 3 mm and thickness of 1.5 mm by electrical discharge machining (EDM). The samples were then polished by polishing cloth with 0.05 μm aluminum-oxides grain to obtain two parallel surfaces of mirror quality to avoid surface effects, such as roughness and unparallel surfaces. The energy dissipated, which result from the roughness and unparallel surface, will lead to the surface effect on nanoindentation [65].

The HEA specimens with the nominal composition of $Al_{0.5}CrCuFeNi_2$, at.%, were investigated in our experiments. Alloys were prepared in a Ti-gettered

high-purity argon atmosphere by arc-melting a mixture of constituent elements with purity higher than 99.9 weight percent (wt.%). The ingot alloys were remelted several times in order to maintain homogeneity, and the molten alloys were drop-cast into a 10 mm diameter copper mold at last. In order to facilitate the microstructure observation and avoid surface the effects, the samples were sequentially polished by polishing cloth with 0.05 μm aluminum-oxides grain, and then the samples etched with the Kalling's reagent.

The structure of the as-cast samples was performed by X-ray diffraction (XRD) with Cu Kα radiation (λ = 1.541874 Å). The microstructures morphology were investigated by using metallographic microscope and a Leo 1525 Field Emission Scanning Electron Microscopy (FE-SEM).

2.2 Nanoindentation tests

The nanoindentation tests were conducted using a Hysitron TriboScope (Minneapolis, MN) attached to a Quesant (Agoura Hills, CA) atomic force microscope (AFM). A non-conducting-diamond NorthStar cubic indenter with a nominal tip radius of 40 nm (Minneapolis, MN) was used. For each loading or loading rate, at least five indents were performed. The indentation depth and indentation load were recorded, and the slope of the upper portion of the unloading curves was used to calculate the contact modulus and indentation hardness. The machine compliance was calibrated to be 1.0 nm/mN. The calculated apparent contact modulus and apparent indentation hardness were statistically analyzed; and the standard deviation for each

condition was used for the error bar in the corresponding diagrams. The typical indentation procedure contains three parts: loading stage (t_L), holding stage (t_H) and unloading stage (t_U) respectively, as shown in Figure 14.

2.2.1 Nanoindentation experiments on BMGs

In order to investigate the effect of different maximum loading on the hardness, reduced contact stiffness and other characteristic, the indentation load ranging from 300, 600, 1,000, 1,500, 2,000, 2,500, 3,000, 5,000 and 8,000 μN was used during the tests. And constant loading and unloading times of 10 second were used in the indentation tests without an intermediate pause between the loading phase and the unloading phase. In order to explore the indentation loading rates dependence of the flow serration in Zr-based bulk metallic glasss under nanoindentation test, with the same peak load, eight loading time and unloading time were used to generate different loading rates. The loading time is range from 1, 2, 5, 10, 20, 40, 80, 160 to 400 s, corresponding to the loading rate of 8, 4, 1.6, 0.8, 0.4, 0.2, 0.1 and 0.05 mNs^{-1}, respectively.

2.2.2 Nanoindentation experiments on HEAs

For the HEA, we only use the indentation load ranging from 1,000, 3,000, 5,000, 7,000 and 9,000 μN during the indentation tests. Constant 10 second was used in the loading and unloading stage of the indentation tests and with an intermediate pause of

10 second between the loading phase and the unloading phase.

2.3 The Stopping and Range of Ion in Matter (SRIM) Simulation of the HEA

SRIM, as one of the most accepted simulation programs in the fields of ion implantation and ion-beam analysis, is widely used for estimating displacement damage and ranges of ions in matter [66, 67, 68]. Since the stopping prediction from SRIM is based on fits to experimental data, it usually provides reasonable predictions. Local dose in displacements per atom (dpa) and ion range distribution of the $Al_{0.5}CrCuFeNi_2$ HEA can be predicted using SRIM 2008.04 full-cascade simulations under the assumptions of a sample density of 7.467 g/cm^3, and threshold displacement energy of 40 eV is assumed for all elements in the SRIM simulation. Both the ion-irradiation-induced disorder profile and ion distribution for certain ion fluence can be estimated.

Chapter 3 Nanoindentation Experiments on BMGs

3.1 Analysis of Nanoindentation Deformation

Due to the plastic flow during nanoindentation, the excessive free volume coalesces in the surface of the metallic glasses and this will change the atomic orders and creates the local stresses in the metallic glasses. The concept of diffusion-induced stresses, which was developed by Yang *et al.* [69], can express that the flow stress and the change of the excessive free volume have the following relationship, and the equation is [70]

$$s = a K \Omega \sqrt{\Delta V} \tag{11}$$

where K is the bulk modulus, σ is the uniaxial flow stress, Ω means the volume of each free volume unit, V is the excessive free volume's concentration and α is a constant related with the Helmholtz free energy and temperature. It is well know that the strain gradient is a determinant role in the deformation behavior of materials by nanoindentation. Thus, the excessive free volume contains two parts, the statistically stored excessive free volume and geometrically necessary excessive free volume. So, the Equation 1 can rewrite as

$$s = a K \Omega \sqrt{\Delta V_S + \Delta V_G} \tag{12}$$

where V_S is the concentration of the statistically stored excessive free volume and V_G is the concentration of the geometrically necessary excessive free volume. For a Berkovich indenter in BMGs, the deformation induced by the indentation is accompanied by the formation and growth of equally distributed triangular loops of strain gradient clusters, as shown in Figure 15 [71]. The Berkovich indenter is

pyramid shape, so, the length of the first triangular loop L_1 is

$$L_1 = 3\sqrt{3}r \tag{13}$$

where *r* defined as the radius of the deformation zone. Similarly, one can obtains

$$L_2 = \frac{h-b}{h} L_1 = \frac{h-b}{h} 3\sqrt{3}r \tag{14}$$

$$L_3 = \frac{h-2b}{h-b} L_2 = \frac{h-2b}{h} L_1 = \frac{h-2b}{h} 3\sqrt{3}r \tag{15}$$

and

$$L_n = \frac{h-(n-1)b}{h-(n-2)b} L_{n-1} = \frac{h-(n-1)b}{h} L_1 = \frac{h-(n-1)b}{h} 3\sqrt{3}r \tag{16}$$

where h is the indentation depth, β defined as the length of the adjacent triangular loops and n defined as $n = h/\beta$. Thus, the total length of the distributed triangular loops can be calculated as

$$L = \sum_1^n L_n = L_1 \left[n - \frac{n(n-1)}{2} \frac{b}{h} \right] \tag{17}$$

Assuming $n = h/b$ **?** 1, so one can obtain that

$$L = \frac{3\sqrt{3}rh}{2b} \tag{18}$$

Schuh *et al.* [72] review some other researchers' work and point out that the hardness for a metallic glass can be defined as $H = h s$, where the value of η is related to the surface profile of the indenter as well as the mechanical properties of the material. For metallic glasses, η is approximate to 3. Thus, the hardness would be

$$s = a h K \Omega \sqrt{\Delta V_S + \frac{9\sqrt{3}\tan^2 q}{16 p b h}} \tag{19}$$

where ΔV_G defined as $\Delta V_G = \frac{9\sqrt{3}\tan^2 q}{16 p b h}$ [70], θ is the angle of the side surface of the

indenter and the material surface. It is well know that $E = 3K(1-2n)$, one can rewrite equation as

$$\frac{H}{E} = \frac{a\,h\Omega\sqrt{\Delta V_S}}{3(1-2n)}\sqrt{1+\frac{h_0}{h}} \tag{20}$$

where E is Young's modulus, v is Poisson's ratio, and h_0 is defined as $h_0 = \frac{9\sqrt{3}\tan^2 q}{16pb\Delta V_S}$. For larger indentation with $h \gg h_0$, thus $h_0/h \approx 0$.

3.2 Deformation Behavior of BMGs

3.2.1 Load-displacement curves

The load-displacement curves for $Zr_{50}Cu_{30}Al_{10}Ni_{10}$ specimen obtained by Berkovich indenter are depicted in Figure 16. Because no bulge behavior is observed during the unloading, this trend means that there is not viscoelastic deformation under the indentation conditions. So, we chose zero second as the holding time in the nanoindentation experiments. From this image, one can easily find that there is a depth increase when the load reaches the maximum. In other words, the depth of the indenter penetrate into the specimen will increase in the ten seconds holding time. The load-displacement curves with different maximum loads overlapped perfectly during the loading stage, and this trend demonstrates that the experimental data have a good reproduction and no surface effects or instability of instrument.

3.2.2 Dependence of the maximum indentation depth on indentation load

In the research of the nanoindentation deformation, one simply uses the Oliver-Pharr approach [1] to analysis the results. However, it is difficult to accurately measuring the size of the pile-up at the submicrometer scale; the effect of the material pile-up is not considered. Figure 17 shows the dependence of the maximum indentation depth on the maximum indentation load with zero second holding time, in which the results were averaged over more than five indentations for each testing condition. From this image, one can easily to find that the depth of the indenter exponential increased with the increasing of the indentation load.

In general, for homogeneous materials, the load-displacement relationships for the indentation load (P) and the elastic displacement of the indenter (h) can be expressed by the following equation [73]:

$$P = K_m h^n \tag{21}$$

where K_m is a constant associated with the elastic behavior of the metallic glasses and n is the index. Kick's Law point out that for all indenters and all geometrically similar indentations, n is postulated equal to 2 when they calculated. Cheng [74] claim that the power law exponent, n, is equal to 2 for a geometrically similar indenter when using dimensional analysis for the geometrically similar indenter. For the three kind of Zr-based BMGs glasses in our experiment, one obtain the exponential index of 1.1, which is different from the value of 2 obtained in Kick and Cheng's work. It has been reported by Schuh *et al.* [72] that the metallic glasses do not obey the maximum-shear stress criterion such as the Tresca or von Mises yield criterion from the growing body

of both experimental and theoretical evidence, even if most all mechanical analyses of indentation problems have been performed these common criteria. Instead, Vaidyanathan *et al.* [75] elucidated in detail that the Zr-based metallic glass exhibit some pressure or normal-stress dependence to their yield criterion, such as the Drucker-Prager yield criterion and the Mohr-Coulomb criterion. So, the von-Mises flow rule is probably inapplicable in the analysis of the deformation behavior of BMG materials and the exponential index, n, in Equation (21) may be different from the value of 2 which obtained from the dimensional analysis based on the von-Mises flow rule [76].

3.2.3 Effect of indentation load on reduced modulus

The dependence of the contact modulus, E_r, on the indentation load with zero seconds holding time is depicted in Figure 18. From this image, one can easily to find that the contact modulus of the three kind of Zr-based BMG alloys decreases with the increase of the indentation load. For the difference between simple tensile and compressive tests and nanoindentation test, a complicated stress field in specimen surface is created in the nanoindentation test due to the contact between indentation tip and specimen surfaces. Due to the nanoindentation coalescience in the shear band, it will generate the excessive free volume and leads to nucleation and formation of voids. The voids in the region subjected to the tensile stress are easily to growth and linkage, so, this will cause less dense packing of atoms and a larger average interatomic spacing. Owing to this reason, the mechanical strength of the specimen

will weakened and the local elastic modulus will reduced. Thus, the decrease of the reduced contact stiffness with the indentation load was caused by the overall effect of the stress-assisted formation of the excessive free volume and the nucleation and formation of voids.

3.2.4 Effect of indentation load on hardness

The dependence of the indentation hardness on the indentation load is depicted in Figure 19. We can also observe that the indentation hardness decreases with the increase of the indentation load, which is similar to the indentation size effect observed in crystalline and polymeric materials. For $Zr_{50}Cu_{40}Al_{10}$ and $Zr_{65}Cu_{18}Ni_7Al_{10}$, they have the same slope of the hardness decrease with the increase of the indentation load; however, the slope of the hardness decrease of $Zr_{50}Cu_{30}Al_{10}Ni_{10}$ is relatively gently.

In general, with the increase of the indentation load, the amount of the excessive free volume and the plastic deformation zone which generated during the indentation loading will also increased. Although more excessive free volume is nucleated during the indentation loading stage, the specific nucleation rate of excessive free volume is lower than the specific growth rate of the plastic zone. Due to this reason, the average concentration of the excessive free volume will decreased.

3.2.5 Effect of loading rate on reduced modulus and hardness

The variation in contact modulus (E_r), hardness (H) and indentation loading rate of the three types of Zr-based BMGs was plotted, as shown in Figures 20 and 21, respectively. We use the model of constant load-rate during the loading and unloading stage in each indentation and the range of the loading rate is from 0.05 to 8 mNs^{-1} for the series of indentation. From this image, one can easily to find that the hardness and reduced modulus exhibit different trends with changing loading rate. For $Zr_{50}Cu_{40}Al_{10}$ and $Zr_{50}Cu_{30}Al_{10}Ni_{10}$ BMGs, there is a bit rise in the reduced modulus as the loading rate is increased from 0.05 to 8 mNs^{-1}, whereas the reduced modulus is a bit decrease of $Zr_{65}Cu_{18}Ni_7Al_{10}$ in this loading rate range. However, the hardness is virtually unchanged throughout the whole range from 0.05 to 8 mNs^{-1}. From the Equation (2), we can find that the hardness is determined from the value P_{max} and A, so, it implies that the A, the project contact area at peak load, is not strongly time-dependent under these experimental conditions. Nevertheless, the elastic modulus is calculated from the slope of the unloading curve, this means that the elastic modulus is sensitive to the loading rate and the recovery is time-dependent under the indentation. The elastic modulus to be sensitive to the loading rate have previously shown by Flores *et al.* [77] in the microhardness measurements on amorphous PET films, the authors find that the loading rate was increased from 0.47 to 13.2 mNs^{-1} will lead to the elastic modulus increased 20% and they attributed to increased viscoelastic recovery at the higher loading rates. However, Beake *et al.* [78] investigated the nanoindentation behavior of the poly film and concluded that with the increasing of the loading rate, the hardness

decreased and the reduced modulus keeps unchanged.

3.2.6 Atomic force microscopy (AFM) image of nanoindentation

Figure 22(a, b) show a typical AFM image of the impression mark obtained after an indentation load of 5,000 μN on the Zr-based BMGs and the corresponding morphological profiles of the residual indentation on the surface of the specimen. As presented in Figure 22(b), it is easily to find that the indentation profiles are self-similar, and a surface pile-up around the indentation. The contact surface of the specimen and the indent tip became wrinkled and highly pile-up, which means greater inhomogeneity flow around the indent. There are about as high as 160 nm pile-up above the average surface level in Zr-based BMGs by quantitative analysis, this also means that the metallic glasses have the severity of local plastic flow during the indentation. The final depth of the contact impression after unloading is about 340 nm, and this is also corresponding to the load-displacement curves, as shown in Figure 16.

Figure 22(c) shows the three-dimensional (3D) image of the nanoindentation deformation, and we can also easily to observe the pile-up around the indentation area. Figure 22(d) presents the image of camera top view during the indentation test.

3.2.7 Evaluation of nanoindentation behavior of BMGs

The function of the reciprocal of the indentation depth and the ratio of the indentation hardness to the reduced contact modulus is plotted, as shown in Figure 23.

Due to the effect of the system stiffness to the reduced contact stiffness is negligible; we can propose that Young's modulus of the metallic glass is proportional to the reduced contact modulus [70]. The data points, which are fitted by a straight line, support the proposed model when we using the reduced contact modulus in Equation (20). From the results of Figure 23, we can conclude that on the nano- and submicrometer scales, the strain gradient contributes to the nucleation and formation of the excessive free volume for the indentation, which is also corresponding to the dependence of the stresses on the variation of the excessive free volume in Equation (2).

Another method of evaluating the indentation behavior of metallic glasses is to analyze the data taken during the indentation test and exploits the dependence of a new parameter hardness/modulus^2 (H/E^2), which suggested by Joslin *et al.* [79].

$$\frac{H}{E_r^2} = \frac{4b^2}{p}\frac{P}{S^2} \tag{22}$$

where β is a constant depending on the indenter geometry. The ratio of H/E^2 is proportional to the indentation load and inversely proportional to the square of the contact stiffness. The dependence of the contact modulus on the indentation load is depicted in Figure 24, from which one concludes that the H/E^2 is a constant independent of the indentation load. This trend means that, for the metallic glasses, the indentation hardness influenced by the indentation-size effect is related to the change of the reduced contact stiffness and the indentation load. The result is also confirms by the observations in Figures 18 and 23.

3.2.8 DSC results of the Zr-based BMGs

DSC measurements were performed to determine characteristic thermal properties, the glass transition temperature (T_g), which is defined as the onset temperature of the endothermic reaction, and the crystallization temperature (T_x), which is defined as the onset value of the exothermic peak. Figure 25 shows the DSC profiles of the three kinds of Zr-based BMGs under the speed heating rate of 20 *K/min*. As shown in this fugure, when we increase the Zr-content, the T_g decreased, which resulting in $\Delta T_x (= T_x - T_g)$ increasing from 64K in $Zr_{50}Cu_{30}Ni_{10}Al_{10}$ up to about 111*K* in $Zr_{65}Cu_{18}Ni_7Al_{10}$.

3.3 Serration-flow Behavior of BMGs

3.3.1 Effect of loading rate on the serration behavior

Nanoindentation load-displacement (*P-h*) curves of Zr-based BMGs at indentation loading rate from 0.02 to 8 mNs-1 are shown in Figure 26(a). For clarity of presentation and focus on the serrated flow, only the loading portions of the load-displacement curves are plotted and all the *P-h* curves are displaced on the same axes with the origins offset 100 nm, except the curve at 8.0 mNs^{-1}, so that multiple curves can be shown on one graph. It is readily seen in Figure 26 that the serrated flow occurs at the slower loading rate (0.4 mNs^{-1} to 0.02 mNs^{-1}) and that the pop-in size gradually increases with the decrease in the loading rate. There is no serrated flow was observed at the loading rate of 0.8 mNs^{-1} or more loading rate. It is also

easily to observe that the pop-in size gradually increases with the increase of the indentation depth, as shown in the slower loading rate curves. About the absence of the serrated flow in the higher loading rates, different researchers have different opinions. Schuh *et al.* [48] proposed that the kinetic limitation for the nucleation of shear bands was the reason of the disappearance of serrated flow at higher loading rates and they also claim that a new homogeneous flow region is exist in the BMGs. Greer *et al.* [80] pointed out that the absence of serrated flow was caused by the instrumental blurring at high loading rates.

Due to the load P is constant in the serrated plastic flow, Yang *et al.* [58] concluded that the the displacement increment at a pop-in event (*Dh*) should have a function with the indentation depth (*h*), and it can be calculated as

$$\Delta h = \frac{24.5\Delta H}{2K_m} h \tag{23}$$

where K_m is a material constant, and *DH* is the hardness reduction. This equation shows that the pop-in size *Dh* is increases linearly with the indentation displacement since the hardness reduction lead to the shear band propagation terminated.

Yang *et al.* [58] research the time duration of the serrated plastic flow at different loading rates, and they point out that the time of each serrated flow was about ~1.4 *ms*, which is independent of the loading rates. Thus, the load increment in 1.4 ms cannot be neglected at higher loading rates, and we can readily observe that *P-h* curves have different slopes in each serrated flow event, not the horizontal lines, as shown in Figure 26(b). It is also easily find that with the decreased of the loading rate, the pop-in slops also decreased, however, the pop-in size increased. The pop-in slop in

the 0.8 mNs^{-1} is very high and it very close to the elastic slop of the P-h curve. Thus, in the higher loading rates, the pop-in event cannot be easily distinguished and it looks like disappear. However, this does not mean that there are no pop-in events (or shear-band emission) in the higher loading rates above 0.8 mNs^{-1}, it is noted that this event still occur in the specimen during indentation.

Form the literature review and results of our experiment; we can conclusion that the shear-band emission is highly affected by the indentation loading rate. Jiang ***et al.*** [81] proposed an explanation about the rate-dependent shear-band behavior in their work, that is temporally intermittent shear-banding operations produce a spatially discrete configuration of a few large shear bands at the lower strain rate, and these large shear band may correspond to simultaneous operations of many fine shear bands. On the country, at the higher strain rate, temporally successive shear-banding operates in front of the plastic zone, which will lead to the spatially dense distribution of many fine shear bands takes the place of shear banding repeatedly at pre-existing shear bands. Li ***et al.*** [82] studies the compressive tests and Vickers microhardness of the BMGs at different temperatures and conclude that both the formation and propagation of the shear bands are related to diffusion and thermally activated processes. Schuh ***et al.*** [83] investigated two kinds of the BMGs and proposed that the formation of the shear bands includes the three steps:

- Stage 1: form a single shear transformation zone (STZ) in the matrix;
- Stage 2: formation of STZ clusters;
- Stage 3: shear band nucleation.

Then, the shear band began to propagation in the specimen.

In Figures 27 and 28, the load-displacement is plotted with different indentation loading rate from 0.02 to 8 $mNs^{-1}$for $Zr_{50}Cu_{30}Al_{10}Ni_{10}$ and $Zr_{50}Cu_{40}Al_{10}$, respectively. It is readily to observed that in $Zr_{50}Cu_{40}Al_{10}$ serrated plastic flow occurs at the slower loading rate (1.6 mNs^{-1} to 0.05 mNs^{-1}) and absence at the higher loading rate (8.0 mNs^{-1} to 4.0 mNs^{-1}). However, there is no serrated plastic flow observed in the $Zr_{50}Cu_{30}Al_{10}Ni_{10}$ during the indentation, even the smallest loading rate 0.02 mNs^{-1}. According to the observation on the plastic zone beneath an indent, Jiang ***et al.*** [81] schematically drawing the cross-section pattern of the plastic zone and shear bands during nanoindentation at lower and higher strain rates, as shown in Figure 29. In front of the plastic zone, shear-banding operations will lead to a configuration of the shear bands, and this is different of the uniaxial compression. During the nanoindentation, the plastic zone beneath an indenter expands radially with the change of time, and the shear banding is accompanied in front of the plastic zone. Thus, the stresses are unevenly distributed in the space during the indentation, and the shear bands spatial distribution is closely related to the temporal characteristic of the shear-banding operations, not the spatial characteristic of the shear-banding operations. As shown in Figure 29(a), a spatially discrete configuration of a few large shear bands was produced by temporally intermittent shear-banding operations at the lower strain rate, and this is corresponding to simultaneous operations of many fine shear bands. However, at the higher strain rate in Figure 29(b), the spatially dense distribution of many fine shear bands generated by the temporally successive shear

banding operations in front of the plastic zone, rather than the shear banding repeatedly at pre-existing shear bands.

3.3.2 Effect of composition on the serration behavior

For readily observed, we choose *P-h* curves with the loading rate of 0.1 $mNs^{-1}$for three kinds of Zr-based BMGs and plotted in one pattern, as shown in Figure 30. In the same loading rate, the serrated plastic flows of the three kinds of BMGs are different, the $Zr_{50}Cu_{40}Al_{10}$ is more pronounced than that for $Zr_{65}Cu_{18}Ni_7Al_{10}$, and however, $Zr_{50}Cu_{30}Al_{10}Ni_{10}$ do not have the serrated plastic flows. Another phenomenon is that the curve on the top of the $Zr_{65}Cu_{18}Ni_7Al_{10}$ is very close to the curve of $Zr_{50}Cu_{40}Al_{10}$ and far away of the $Zr_{50}Cu_{30}Al_{10}Ni_{10}$. Due to the *P-h* curves are displaced on the same axes with the origins offset 150 nm, the final load depth of the $Zr_{65}Cu_{18}Ni_7Al_{10}$ is greater than $Zr_{50}Cu_{40}Al_{10}$ and $Zr_{50}Cu_{30}Al_{10}Ni_{10}$. This trend means that the hardness of the $Zr_{65}Cu_{18}Ni_7Al_{10}$ is bigger than $Zr_{50}Cu_{40}Al_{10}$ and $Zr_{50}Cu_{30}Al_{10}Ni_{10}$, which corresponding the results in Figure 19. The significant difference of the three Zr-based metallic glasses reflects their microstructures, in terms of free volume, and short and middle-range ordering are dissimilarity. As shown in Figure 19 and Figure 30, the hardness and reduced modulus of $Zr_{65}Cu_{18}Ni_7Al_{10}$ is smaller than $Zr_{50}Cu_{40}Al_{10}$, and that the plastic flow of former alloy shows less serration than the latter. The basic principle for this phenomenon is not well understood at this moment, but will be deep research in the future. Liu *et al.* [83] test two Zr-based metallic glasses and concluded that the serrated flow is closely

related to these innate properties. They point out that smaller modulus and hardness lead to a smaller atomic binding strength and a looser topological structure, which means a higher free volume in an amorphous structure. Due to the serrated plastic flow are related to the shear bands activity, which usually formed in the sites of more free volume, then cause to the serrated plastic flow during indentation. However, this explanation is contradicting to our results, so, the reason of this phenomenon need more in-depth study.

3.3.3 The relationship between pop-in size and indentation depth

It is easily to find that the pop-in size and the indentation depth have the linear relationship, with the increase of the indentation depth, the pop-in size also increased, as shown in Figure 31. Schuh *et al.* [44] and Greer *et al.* [80] have reported this phenomenon and they explained as ‘‘length scaling’’. They point out that the larger pop-ins lead to greater shear displacements within the shear band, because a single shear band can produce several microns displacements. Thus, the total number of the pop-in events will decrease with the same amount of indentation displacement, and is the reason why the fewer pop-in events in the deeper indentation depth.

3.3.4 The relationship between strain rate and indentation depth

According to the Sargent and Ashby’s research [84], the displacement rate is a non-linear function of time during an indentation with a constant loading rate, which

means the indentation strain rate can be defined as:

$$\dot{\varepsilon}_i = \frac{1}{h}\frac{dh}{dt} \tag{24}$$

where h is the indenter displacement during indentation. The instantaneous indentation strain rate is plotted at 0.4, 1.6 and 8.0 mNs^{-1} as a function of the indentation depth for $Zr_{50}Cu_{40}Al_{10}$ and plotted at 0.1, 0.4 and 1.6 mNs^{-1} as a function of the indentation depth for $Zr_{65}Cu_{18}Ni_7Al_{10}$ in Figures 32(a) and (b), respectively. For the clarity of observation, except the curve at the strain rate of 0.4 mNs^{-1} in Figure 32(a) and 0.1 mNs^{-1} in Figure 32(b), all the other curves are plotted on the same axes with the strain rates offset by one order of magnitude. Due to the equation is singular at $h=0$, the strain rate is effectively infinite at the outset of each experiment. However, with the indentation depth increased, the strain rate decreased as ~1/h and eventually approaches an approximately constant value at a large indentation depth. There are several obvious strain rate spikes at each indentation rate and the strain rate sizes appear to increasing with the indentation proceeds. The strain rate peaks highlight and corresponding exactly with the pop-in events or the displacement serrations in the load-displacement curves in Figures 26 and 27. One can also observed that for the same indentation strain rate, such as 0.4 mNs^{-1}, these peaks are more pronounced in the $Zr_{50}Cu_{40}Al_{10}$ than the $Zr_{65}Cu_{18}Ni_7Al_{10}$, and their magnitude is strongly affected by the indentation strain rate.

3.3.5 The relationship between displacement and time

Figure 33 shows a typical curve of the indenter displacement versus time (*h-t*), which is obtained from the $Zr_{50}Cu_{40}Al_{10}$ at the loading rate of 0.1 mNs^{-1}. In order to evidently observation, we cut out a section of the h-t curve and plotted as insertion shows. Here, τ is defined as the time duration or of a pop-in event. Li *et al.* [85] developed a simple protocol to identify the pop-in event, and to distinguish them from the noise. The low-frequency and high-amplitude signal is clearly the real pop-in events representing the jumpy plastic deformation of the metallic glass, but the high-frequency and low-amplitude signal is the machine's noise floor. Li *et al.* [85] point out that there are three stages can be used to identify the pop-in events. A maximum homogeneity smoothing technique was used in the first stage which involves a data smoothing algorithm to filtering out the noise and obtains the original configuration of the curve. The second stage makes use of a median smoothing technique to filtering out the noise with same method of the first stage. The third stage uses a burst search algorithm to detect and record the pop-in data throughout the whole *h-t* curve according to the pre-set values.

3.3.6 The consolidated elastic curve

A single serrated *P-h* curve obtained at a loading rate of 0.1 mNs^{-1} on the $Zr_{50}Cu_{40}Al_{10}$ BMGs alloy, including the elastic unloading section of the curve, is shown in Figure 34. The recovered elastic depth, $h_{plastic}$, is observed about 393 nm after removal of the indenter tip. Gouldstone *et al.* [86] proposed a interesting method,

which is assess the contribution of discrete shear bands to plastic deformation of the alloy, and describe the construction of a ‘‘consolidated elastic’’ loading curve, which obtained by removing all of the pop-in gap from the loading stage of the ***P-h*** curve. As illustrated by the arrows in Figure 34, a smooth and continuous curve was obtained by the Gouldstone ***et al.***’s method, which can essentially corrects the experimental ***P-h*** curve by remove the total depth of the serrated flow ($h_{pop\text{-}in}$). At the maximum loading, we can clearly observed that the depth of the $h_{pop\text{-}in}$ is about 214.5 nm, the depth of the ‘‘consolidated elastic’’ h_{real} is equal to 281.44 nm, and the true elastic depth is about 102 nm. For different materials, they exhibit different results of these experiment results. In the work of the Schuh ***et al.*** [44], the value of the h_{real} is close to the $h_{elastic}$ and they point out that due to the motion of individual shear bands, the plastic strain experienced by the Pd-30Cu-10Ni-20P (at %) during nanoindentation occurs in discrete bursts. However, in the indentation tests of La-25Al-10Cu-5Ni-5Co (at %) BMG alloy investigated by Nieh and Schuh ***et al.*** [87], the value of the h_{real} is approximately three times of the $h_{elastic}$. The ratio of the h_{real} and $h_{elastic}$ is nearly about 2.8, which is very close to the ratio in the La-25Al-10Cu-5Ni-5Co BMG alloy.

3.4 Conclusions

The deformation behavior of the metallic glasses is inhomogeneous and serrated flow was observed in the indentation experiments. From the investigated of the deformation behavior and the serrated flow behavior in the Zr-based BMGs, we can

conclude that:

The load-control mode was used in the indentation experiment and both the indenter hardness and reduced modulus of the three kinds Zr-based BMGs decreased with the increase of the indentation load.

With the increasing of the loading rate in the indentation experiment, the reduced modulus of both $Zr_{50}Cu_{40}Al_{10}$ and $Zr_{50}Cu_{30}Al_{10}Ni_{10}$ BMGs were increased and $Zr_{65}Cu_{18}Ni_7Al_{10}$ was decreased. However, the hardness of the three kinds of Zr-based BMGs was kept constant when the loading rates increased in the indentation experiments.

From the AFM image of the impression mark obtained after an indentation load, we can readily find that the indentation profiles are self-similar, and a surface pile-up around the indentation. The contact surface of the specimen and the indent tip became wrinkled and highly pile-up, which means greater inhomogeneity flow around the indent.

The serration flow was observed in the indentation experiment in both $Zr_{50}Cu_{40}Al_{10}$ and $Zr_{65}Cu_{18}Ni_7Al_{10}$ BMGs. However, no serration flow was revealed in the $Zr_{50}Cu_{30}Al_{10}Ni_{10}$ BMG. Increasing with the loading rate, the pop-in size decreased and the serration behavior became weak, then it disappears in the higher loading rates.

Chapter 4 Nanoindentation Tests and Irradiation Simulation on HEA

4.1 XRD Results of HEA

Figure 35 illustrates the XRD patterns of as-cast $Al_{0.5}CrCuFeNi_2$ alloys which are identified crystalline structure. The picks of the (111), (200) and (220) shown that this HEA basically belong to fcc structure. The small peaks slightly on the left of the matrix fcc of $Al_{0.5}CrCuFeNi_2$ in XRD curve is identified as Cu-rich interdendrites, which have the same location of copper. Guo *et al.* [88] investigated a series of $Al_xCrCuFeNi_2$ alloys and point out that at $x < 0.7$, the HEA alloy is fcc structure; at $0.8 < x < 1.8$, the HEA alloy is fcc+bcc structure; and when $1.8 < x$, fcc solid solutions could not be detected, which means that the HEA alloy is bcc structure.

4.2 SEM Analysis of HEA

4.2.1 SEM image of HEA

A typical SEM image the as-cast $Al_{0.5}CrCuFeNi_2$ sample is shown in Figure 36. As shown in this image, one can readily to observation that the HEA specimen has two phases, which are indicated as dark gray area and light grey area, respectively. The microstructure of the HEA alloys showed a typical dendritic structure, the fcc dendrite phase which contains the poly-grained fcc matrix phase (dark gray area) and the fcc Cu-rich interdendritic phase which consists of the poly-grained fcc Cu-rich

phase (light grey area) [89, 90, 91].

4.2.2 EDS results of HEA

The two phases are clearly visible in Figure 37(a) on the polished HEA surface. In order to identify composition of the different phase, the elemental concentration analysis was examined by EDS. As shown in Figure 37, the white (b), red (c), purple (d), yellow (e), and blue (f) maps correspond to aluminum, chromium, copper, iron, and nickel, respectively. It is observed that copper atoms (Figure 37(d)) concentrate in the light grey area, suggesting that this grey area contains higher concentration of copper than the dark gray area. For the element of chromium, iron, and nickel, shown as the red [Figure 37(c)], yellow [Figure 37(e)], and blue [Figure 37(f)] color, higher concentration of these elements are found in the dark grey area rather than the light grey area. Relatively, the element of aluminum has uniform concentration as compared to the other elements.

The chemical composition analysis of the different phase was performed by EDS (Figure 38). The analysis is carried out from 5 different locations, two in the light grey area and three in the dark gray area to achieve more reliable results. As shown Figure 38, the result of the point A is shown on the top right and the result of the point D is shown on the bottom right. Elements concentration in the different region and the nominal element concentration are summarized in Table 3. In the light grey area, denoted by the points A and B, the copper concentrations are 55.41% and 51.20%, approximately three times of the estimated copper concentration. Furthermore, the

aluminum concentration is more than the estimated aluminum concentration. On the contrary, the concentration of the chromium, iron, and nickel is lower than their estimated concentration. In the dark gray area, the concentration of the copper and aluminum in the points of C, D, and E is less than their estimated concentration. Conversely, the concentration of the chromium, iron, and nickel are all higher than their estimated concentration. As a summary, the composition of the light gray area is approximately $Al_{11.7}Cr_{7.5}Cu_{53}Fe_6Ni_{21.8}$, at.%, and the dark gray area is approximately $Al_{7.7}Cr_{20}Cu_{13.4}Fe_{20.7}Ni_{38.2}$, at.%. All of these results are in agreement with the elemental mapping results in Figure 37.

4.3 Deformation behavior of HEA

4.3.1 AFM image of HEA

Figure 39 shows a typical AFM image of the impression mark obtained after an indentation load of 5,000 μN on the $Al_{0.5}CrCuFeNi_2$ HEA and the corresponding morphological profiles of the residual indentation on the surface of the specimen. It is readily to find that a surface pile-up around the indentation, as shown Figure 39(b). Compare to the high of 160 nm pile-up above the average surface level in Zr-based BMGs by quantitative analysis, the $Al_{0.5}CrCuFeNi_2$ HEA only have 120 nm pile-up above the average surface level when they use the same indentation load, which also means that the $Al_{0.5}CrCuFeNi_2$ HEA have the lower hardness than the Zr-based BMGs and this is also corresponding to the results from Figure 41 and Figure 19. The

final depth of the contact impression after unloading is about 350 nm, which is almost the same with the Zr-based BMGs' contact impression depth. Figure 39(c) shows the 3 dimensions (3D) image of the nanoindentation deformation and the pile-up around the indentation area are readily observed. Figure 39(d) is the image of camera top view during the indentation test.

4.3.2 Load-displacement curves of HEA

Figure 40 display the typical load-displacement curves at different peak indentation load on the $Al_{0.5}CrCuFeNi_2$ HEA. A considerable amount of creep strain was found for the entire different indentation load, this means that the $Al_{0.5}CrCuFeNi_2$ HEA exhibit viscoelastic behavior under the indentation conditions. Thus, the holding section is necessary for the dissipation of creep displacement at the peak and we chose ten seconds as the holding time in the indentation experiments. It is clearly observed that no cracks were formed during indentation, which is means no serration behavior in the $Al_{0.5}CrCuFeNi_2$ HEA. The load-displacement curves with different maximum loads also overlapped perfectly during the loading stage, and this demonstrates that the experimental data have a good reproduction and no surface effects or instability of instrument.

4.3.3 Effect of indentation load on the reduced modulus and hardness

Figure 41 shows the function between the indentation load and the contact modulus (left axis) and the indentation load and the hardness (right axis) of th contact e $Al_{0.5}CrCuFeNi_2$ HEA, and it also shown that the both the contact modulus and hardness have a strong load-dependence. It is easily observed that both the contact modulus and hardness decreased with the increasing of the indentation load. The indentation size effect lead to the higher hardness and modulus at lower indentation load, and this phenomenon is occur in most materials [92]. The high values of the contact modulus (177GPa) and hardness (7GPa) are decreased to 155 GPa and 4 GPa, respectively. And at the higher indentation load (P > 5000μN), the value of the contact modulus and hardness get very closer.

4.4 Irradiation Analysis of HEA

4.4.1 Parameter setting of irradiation simulation

The as-cast HEAs samples of $Al_{0.5}CoCrFeNi_2$ are prepared, and the density measured by the drainage method is 7.467 g/cm^3. In order to predict the energy-dependent penetration depth of heavy ions, Au ions with the energy ranging from 0.05 to 20 MeV are calculated. The SRIM-predicted ion range is summarized in Figure 42. The result shows that with increasing the energy of the incident ions, the ion range also increases. When the incident ion energy is 10 MeV, the ion range is 1 μm. To better estimate the displacement damage, 10 MeV Au is chosen for the full

collision cascade simulation. In order to predict the maximum reachable dose, dose and ion profiles are calculated, assuming under optimized irradiation conditions and long irradiation time of 10 hours. Detailed information is listed in the Table 4, together with the SRIM simulation results.

4.4.2 Irradiation of Au in HEA

Figure 43 shows the calculated depth-dependent displacement damage and implanted ion profiles by SRIM for 10 MeV Au-irradiated HEA and for the ion fluence of 2.0×10^{16} Au/cm^2. These results were obtained from Monte Carlo simulations using the SRIM-2008.04 full-cascade mode, in which the calculations were carried out under the assumptions of a sample density of 7.467 g/cm^3 and threshold displacement energies of 40 eV for every element. The predicted dose maximum is 158.76 dpa, and the damage level above 40 dpa ranges from 0 to ~ 1,300 nm. The highly-damaged region (above ~ 80 dpa) expands from 300 to 1,200 nm with the damage peak at 900 nm. In the surface region of the specimen, the damage dose is about 50 dpa. However, with the increase of the depth, the damage dose increased rapidly. And it also decreased quickly from the maximum to the 0 dpa, when the depth is larger than 1500 nm. The rapid increase and decrease of the damage dose in the specimen indicate that the Au irradiation produces non-uniform damage. Moreover, as shown in Figure 43, the maximum concentration of Au is approximately 0.49% (at.%) at a depth of 1,060 nm, which is somewhat greater than the depth of the maximum damage dose as expected, and the calculated full width at half maximum for the

implanted ion distribution is 460 nm for 10 MeV Au ions. In order to obtain the approximate 100 dpa damage in the proposed HEA samples, 10 MeV Au to the fluence of 1.5×10^{16} cm^{-2} may be used to create radiation damage.

4.4.3 Irradiation of Co in HEA

The profiles of damage and Co concentration are calculated by SRIM full-cascade simulations in the HEA under 10 MeV Co irradiation for an ion fluence of 2.0×10^{16} Co/cm^2, assuming the average displacement energy of 40 eV for all of the elements in the HEA and in this research, as shown in Figure 44. In this study, the predicted dose maximum is approximately 41.57 dpa. The highly-damaged region (above 25 dpa) ranged from 1,400 to 2,400 nm, and the damage peak is approximately 2,100 nm. The Co profile is also shown in Figure 44, where the calculated concentration maximum is 0.436% (at.%) at the depth of 2,300 nm, and the calculated full width at half maximum for the implanted ion distributions is 485 nm for 10 MeV Co ions. At depths midway between the surface and implanted Co-ion regions, the calculated implanted Co concentration is negligible, and the calculated displacement damage is about half of the peak damage level.

4.5 Conclusions

The XRD patterns of as-cast $Al_{0.5}CrCuFeNi_2$ alloys reveal that the crystalline structure of this HEA was an fcc structure.

The HEA specimen has two phase sand showed a typical dendritic structure, the fcc dendrite phase which contains the poly-grained fcc matrix phase and the fcc Cu-rich interdendritic phase which consists of the poly-grained fcc Cu-rich phase. And this result is also corresponding to the EDS analysis.

Both the contact modulus and indentation hardness of the $Al_{0.5}CrCuFeNi_2$ alloys have a strong load-dependence and they were both decreased with the increasing of the indentation load.

Based on the results of the SRIM simulation, we establish the relationship between the ion energy and ion range from the SRIM simulation. The Au and Co irradiation simulation reveal that the highly-damaged region is around from 200 to 1,200 nm and from 1,400 to 2,400 nm for the Au-irradiated and Co-irradiated samples, respectively.

Chapter 5 Conclusions

The nanoindentation experiments on the $Zr_{50}Cu_{40}Al_{10}$, $Zr_{50}Cu_{30}Al_{10}Ni_{10}$ and $Zr_{65}Cu_{18}Ni_7Al_{10}$ BMG alloys were performed at different loading (300 μN $\sim$ 8000 μN) and different loading rates (0.02 mNs^{-1} $\sim$ 8 mNs^{-1}). The deformation behavior and the serration behavior of the three kinds of Zr-based BMGs were investigated with a load-control mode and the data were compared. Both the indenter hardness and reduced modulus of the three kinds of Zr-based BMGs decreased with the increase of the indentation load. However, they have different trend with the change of the loading rate, such as the constant hardness in the different loading rates.

The serration flow was observed in the indentation experiment in both $Zr_{50}Cu_{40}Al_{10}$ and $Zr_{65}Cu_{18}Ni_7Al_{10}$ BMGs. However, no serration flow was revealed in the $Zr_{50}Cu_{30}Al_{10}Ni_{10}$ BMG. Serration-flow behavior was strongly associated with the shear-band emission and dependent on the loading rate in the nanoindentation experiments. It was also observed that the serration-flow behavior occurs at lower loading rates but disappeared at the higher loading rate. However, this trend does not mean that there are no serration flow in the higher loading rates, it is noted that this event still occur in the specimen during indentation.

The morphological profiles of the residual indentation on the surface of the specimen after an indentation were observed by the AFM, and the DSC measurements were performed to determine characteristic thermal properties, the glass-transition temperature (T_g), and the crystallization temperature (T_x).

The deformation behavior in the $Al_{0.5}CrCuFeNi_2$ HEA was also investigated using the nanoindentation test at different load. The indenter hardness and reduced modulus of the $Al_{0.5}CrCuFeNi_2$ HEA decreased with the increase of the indentation load. However, no serration behavior was observed during the indentation experiment. Creep behavior was observed in the indentation tests because the HEA exhibits viscoelastic behavior under the indentation conditions.

The microstructure of the HEA was investigated by the XRD, AFM, SEM, and EDS. For the advanced research, the ion implantation simulation of the HEA was preformed. Based on the results of the SRIM simulation, we establish the relationship between the ion energy and ion range from the SRIM simulation. The Au and Co irradiation simulation reveals that the highly-damaged region is from 200 to 1,200 nm and from 1,400 to 2,400 nm for the Au-irradiated and Co-irradiated samples, respectively.

Chapter 6 Future Work

In order to further understand the deformation behavior and the serration-flow characteristics of the BMGs and HEAs, and reveal the misunderstanding or debates on the nanoindentation, such as the origin of the serration flow and the site of a shear band formed, there are still a lot of work should be down in the future, which is listed as follows:

(1) It is widely accepted that the serration flow is associated with the shear-band emission. However, deep research should be done to reveal that how the shear-band influences the serration-flow behavior and the fundamental origins of the shear band.

(2) This thesis investigated the deformation behavior and the serration-flow characteristics of BMGs and HEAs at room temperature. However, there will have totally different deformation and serration-flow behavior in the high temperature. So, the nanoindentation experiment at higher temperatures should be performed to characterize the deformation and serration-flow behavior.

(3) Anti-corrosion is a very important aspect in the application of BMGs and HEAs. So, the investigation of the deformation and serration-flow behavior in the nanoindentation experiment under a corrosion condition must be very interesting in the future, and these studies are also very important in the application of BMGs and HEAs.

(4) Potential applications of HEAs in advanced nuclear-energy systems will require materials that can withstand extreme reactor environments of high-temperature and high-doses radiation. So, the investigation of the change of the mechanical properties before and after ion irradiation is very important in the HEAs' research. My thesis only investigated the deformation and serration-flow behavior of the as-cast HEAs, and the nanoindentation experiment of the irradiated specimen should be performed in the next stage.

List of References

[1] W.C. Oliver, and G.M. Pharr. *An improved technique for determining hardness and elastic modulus using load and displacement sensing indentation experiments.* Journal of Materials Research, 7(1992), pp. 1564-1583.

[2] W.C. Oliver, and G.M. Pharr. *Measurement of hardness and elastic modulus by instrumented indentation: Advances in understanding and refinements to methodology.* Journal of Materials Research, 19 (2004), pp. 3-20.

[3] S.I. Bulychev, V.P. Alekhin, M.K. Shorshorov, A.P. Ternovskii, and G.D. Shnyrev. *Determining Young's modulus from the indentor penetration diagram.* Zavodskaya Laboratoriya, 41 (1975), pp. 1137-1140.

[4] A.P. Ternovskii, V.P.Alekhin, M.K.Shorshorov, M.M.Khrushchov, and V.N.Skvortsov. *Micromechanical testing of materials by depression.* Zavodskaya Laboratoriya, 39(1974), pp. 1242-1247.

[5] B. Poon, D. Rittel, and G. Ravichandran. *An analysis of nanoindentation in linearly elastic solids.* International Journal of Solids and Structures, 45 (2008). pp. 6018-6033.

[6] B. Bhushan, and V.N. Koinkar. *Nanoindentation hardness measurements using atomic force microscopy.* Applied Physics Letters, 64(1994), pp. 1653-1655.

[7] E.K. Dimitriadis, F. Horkay, J. Maresca, B. Kachar, and R.S.Chadwick. *Determination of elastic moduli of thin layers of soft material using the atomic force microscope.* Biophysical Journal, 82(2002), pp. 2798-2810.

[8] M.R. VanLandingham, J.S. Villarrubia, W.F. Guthrie, and G.F.Meyers. *Nanoindentation of polymers: an overview. Iin: V.V. Tsukruk, N.D. Spencer eds, Advances in Scanning Probe Microscopy of Polymers.* Macromolecular Symposia, 167(2001). pp. 15-43.

[9] C.E. Carltona, and P.J. Ferreirab. *In situ TEM nanoindentation of nanoparticles.* Micron, 43(2012), pp. 1134-1139.

[10] E. Le Bourhisa, and G. Patriarcheb. *TEM-nanoindentation studies of semiconducting structures.* Micron, 38(2007), pp. 377-389.

[11] A.J. Lockwood, and B.J. Inkson. *In situ TEM nanoindentation and deformation of Si-nanoparticle clusters.* Journal of Physics D: Applied Physics, 42(2009), pp. 1-5.

[12] B. Lucas and W. Oliver. *Indentation Power-Law Creep of High-Purity Indium.* Metallurgical and Materials Transactions A, 30 (1999), pp. 601-610.

[13] B. Poon, D. Rittel, and G. Ravichandran. *An analysis of nanoindentation in linearly elastic solids.* International Journal of Solids and Structures, 45(2008), pp. 6018-6033.

[14] microstartech.com; Available from: http://www.microstartech.com/.

[15] G. Simmons, H. Wang. Single Crystal Elastic Constants and Calculated Aggregate Properties: A Handbook. Cambridge, MA, 1971. MIT Press.

[16] J.L. Hay, and G.M.Pharr. *Instrumented indentation testing.* ASM Handbook, 8(2000), pp. 232-243.

[17] W. Klement, R.H. Willens, and P. Duwez. *Non-crystalline structure in solidified gold–silicon alloys.* Nature, 187(1960), 869-870.

[18] H. S. Chen, and C. E. Miller. *Centrifugal spinning of metallic glass filaments.* Materials Research Bulletin. 11(1976), pp. 49-54.

[19] H.S. Chen. *Glassy metals.* Reports on Progress in Physics, 43(1980), pp. 353-432.

[20] A.J. Drehman, A.L. Greer, and D. Turnbull. *Bulk formation of a metallic glass: $Pd_{40}Ni_{40}P_{20}$.* Applied Physics Letters, 41(1982), pp. 716-717.

[21] H.W. Kui, A.L. Greer, and D. Turnbull. *Formation of bulk metallic glass by fluxing.* Applied Physics Letters, 45(1984), pp. 615-616.

[22] A. Inoue, T. Zhang, and T. Masumoto. *Zr-Al-Ni amorphous alloys with high glass transition temperature and significant supercooled liquid region.* Materials Transations, JIM, 31(1990), pp. 177-183.

[23] A. Peker, and W.L. Johnson. *A highly processable metallic glass: $Zr_{41.2}Ti_{13.8}Cu_{12.5}Ni_{10.0}Be_{22.5}$.* Applied Physics Letters, 63 (1993), pp. 2342-2344.

[24] A. Inoue. *Stabilization of metallic supercooled liquid and bulk amorphous alloys.* Acta Materialia, 48,(2000), pp. 279-306.

[25] M.E. Siegrist, and J.F. Löffler. *Bulk metallic glass-graphite composites.* Scripta Materialia, 56(2007), pp. 1079-1082.

[26] D. Turnbull. *Under what conditions can a glass be formed?* Contemporary Physics, 10(1969), pp. 473-488.

[27] D. Turnbull. *Metastable structures in metallurgy.* Metallurgical and Materials Transactions B, 12 (1981), pp. 217-230。

[28] B. Yang, Y. Du, and Y. Liu. *Recent progress in criterions for glass forming ability.* Transactions of Nonferrous Metals Society of China, 19(2009), pp. 78-84.

[29] S.J. Pang, T. Zhang, K. Asami, and A. Inoue. *Synthesis of Fe-Cr-Mo-C-B-P bulk metallic glasses with high corrosion resistance.* Acta Materialia, 50(2002), pp. 489-497.

[30] A. Inoue. *High strength bulk amorphous alloys with low critical cooling rates.* Materials Transactions, 36(1995), pp.866-875.

[31] T.A. Waniuk, J. Schroers, and W.L. Johnson. *Critical cooling rate and thermal stability of Zr-Ti-Cu-Ni-Be alloys.* Applied Physics Letters, 78(2001), pp. 1213-1215.

[32] A. Inoue, W. Zhang, T. Zhang, and K. Kurosaka. *High-strength Cu-based bulk*

glassy alloys in Cu-Zr-Ti and Cu-Hf-Ti ternary systems. Acta Materialia, 49(2001), pp. 2645-2652.

[33] T.D. Shen, Y. He, and R.B. Schwarz. *Bulk amorphous Pd-Ni-Fe-P alloys: Preparation and characterization.* Journal of Materials Research, 14(1999), pp. 2107-2115.

[34] T.D. Shen and R.B. Schwarz. *Bulk ferromagnetic glasses prepared by flux melting and water quenching.* Applied Physics Letters, 75(1999), pp. 49-51.

[35] Z.P. Lu and C.T. Liu. *A new glass-forming ability criterion for bulk metallic glasses.* Acta Materialia, 50(2002), pp. 3510-3512.

[36] Z.P. Lu and C.T. Liu. *Glass formation criterion for various glass-forming systems.* Physical Review Letters, 91(2003), p. 115505.

[37] Z.P. Lu and C.T. Liu. *A New approach to understanding and measuring glass formation in bulk amorphous materials.* Intermetallics, 12(2004), pp. 1035-1043.

[38] G.J. Fan, H. Choo, and P.K. Liaw. *A new criterion for the glass-forming ability of liquids.* Journal of Non-Crystalline Solids, 353(2007), pp.102-107.

[39] Q. Chen, J. Shen, D. Zhang, H. Fan, J. Sun, and D.G. Mccartney. *A new criterion for evaluating the glass-forming ability of bulk metallic glasses.* Materials Science and Engineering: A, 433(2006), pp. 155-160.

[40] Z. Yuan, S. Bao, Y. Lu, D. Zhang, and L. Yao. *A new criterion for evaluating the glass-forming ability of bulk glass forming alloys.* Journal of Alloys and Compounds, 459(2008), pp. 251-260.

[41] K. Amiya and A. Inoue. *Fe-(Cr, Mo)-(C, B)-Tm bulk metallic glasses with high, strength and high glass-forming ability.* Reviews on Advanced Materials Science, 18(2008), pp. 27-29.

[42] A. Inoue, B. Shen, H. Koshiba, H. Kato, and A.R. Yavari. *Cobalt-based bulk*

glassy alloy with ultrahigh strength and soft magnetic properties. Nature Materials, 2(2003), pp. 661-663.

[43] V.L-L. Dmitri, V.L-L. Larissa, and Y.C. Alexander. *Mechanical properties and deformation behavior of bulk metallic glasses.* Metals, 3(2013), pp. 1-22.

[44] C.A. Schuh and T.G. Nieh. *A nanoindentation study of serrated flow in bulk metallic glasses.* Acta Materialia, 51(2003), pp. 87-99.

[45] M. Miller and P.K. Liaw. *Bulk Metallic Glasses.* Springer, 2008.

[46] W.H. Jiang, G.J. Fan, H. Choo, and P.K. Liaw. *Ductility of a Zr-based bulk metallic glass with different specimen's geometries.* Materials Letters, 60(2006), pp. 3537-3540.

[47] J.-J. Kim, Y. Choi, S. Suresh, and A.S. Argon. *Nanoindentation of a bulk amorphous metal alloy at room temperature.* Science, 295(2002), pp. 654–657.

[48] C.A. Schuh, A.C. Lund, and T.G. Nieh. *New regime of homogeneous flow in the deformation map of metallic glasses: elevated temperature nanoindentation experiments and mechanistic modeling.* Acta Materialia, 52(2004), pp. 5879-5891.

[49] R.D. Conner, Y. Li, W.D. Nix, and W.L. Johnson. *Shear band spacing under bending of Zr-based metallic glass plates.* Acta Materialia, 52(2004), pp. 2429-2434.

[50] G.Y. Wang, P.K. Liaw, W.H. Peter, B. Yang, Y. Yokoyama, M.L. Benson, B.A. Green, M.J. Kirkham, S.A. White, T.A. Saleh, R.L. McDaniels, R.V. Steward, R.A. Buchanan, C.T. Liu, and C.R. Brooks. *Fatigue behavior of bulk metallic glasses.* Intermetallics, 12(2004), pp. 885-892.

[51] Y.I. Golovin, V.I. Ivolgin, V.A. Khonik, K. Kitagawa, and A.I. Tyurin. *Serrated plastic flow during nanoindentation of a bulk metallic glass.* Scripta

Materialia, 45 (2001), pp. 947-952.

[52] C.A. Schuh, T.G. Nieh, and Y. Kawamura. *Rate dependence of serrated flow during nanoindentation of a bulk metallic glass.* Journal of Materials Research, 17(2002), pp. 1651-1654.

[53] J.G. Wang, B.W. Choi, T.G. Nieh, and C.T. Liu. *Crystallization and nanoindentation behavior of a bulk Zr-Al-Ti-Cu-Ni amorphous alloy.* Journal of Materials Research, 15(2000), pp. 798-807.

[54] W.J. Wright, R. Saha, and W.D. Nix. *Deformation mechanisms of the $Zr_{40}Ti_{14}Ni_{10}Cu_{12}Be_{24}$ bulk metallic glass.* Materials Transactions, 42 (2001), pp. 642-649.

[55] H. Kimura, and T. Masumoto. *A model of the mechanics of serrated flow in an amorphous alloy.* Acta Materialia, 31(1983), pp. 231-240.

[56] T. Mukai, T.G. Nieh, Y. Kawamura, A. Inoue, and K. Higashi. *Influence of strain rate on compressive mechanical behavior of $Pd_{40}Ni_{40}P_{20}$ bulk metallic glass.* Intermetallics, 10(2002), pp. 1071-1077.

[57] C.A. Schuh, T.G. Nieh, and Y. Kawamura. *Rate dependence of serrated flow during nanoindentation of a bulk metallic glass.* Journal of Materials Research, 17(2002), pp. 1651-1654.

[58] B. Yang, and T.G. Nieh. *Effect of nanoindentation rate on the shear band formation in an. Au-based bulk metallic glass.* Acta Materialia, 55(2007), pp. 295-300.

[59] W.H. Jiang, and M. Atzmon. *Rate dependence of serrated flow in a metallic glass.* Journal of Materials Research, 18 (2003), pp. 755-757.

[60] Y. Zhang, X. Yang, and P.K. Liaw. *Alloy Design and Properties Optimization of High-Entropy Alloys.* JOM, 64(2012), pp. 830-838.

[61] M.A. Hemphill, T. Yuan, G.Y. Wang, J.W. Yeh, C.W. Tsai, A. Chuang, and P.K.

Liaw. *Fatigue behavior of $Al_{0.5}CoCrCuFeNi$ high entropy alloys.* Acta Materialia, 60(2012), pp. 5723-5734.

[62] Y. Zhang, Y.J. Zhou, J.P. Lin, G.L. Chen, and P.K. Liaw. *Solid Solution Phase Formation Rules for multicomponent Alloys.* Advanced Engineering Materials, 10(2008), pp. 534-538.

[63] B. Cantor, I.T.H. Chang, P. Knight, and A.J.B. Vincent. *Microstructural development in equiatomic multicomponent alloys.* Materials Science and Engineering: A, 375-377 (2004), pp. 213-218.

[64] O.N. Senkov, G.B. Wilks, D.B. Miracle, C.P. Chuang, and and P.K. Liaw. *Refractory high-entropy alloys.* Intermetallics, 18(2010), pp. 1758-1765.

[65] H. Li, A. Ghosh, Y.N. Han, and R.C. Bradt. *The frictional component of the indentation size effect in low load microhardness testing.* Journal of Materials Research. 8(1993), pp. 1028-1032.

[66] F.J. Ziegler, J.P. Biersack, and M.D. Ziegler. *SRIM-The Stopping and Range of Ions in Solids(SRIM Co., Chester, MD, 2008); as well as the original book of by J. F. Ziegler, J. P. Biersack, and U. Littmark* (Pergamon, New York, 1985).

[67] M.K. Miller and Y. Zhang. *Fabrication and characterization of APT specimens from high dose heavy ion irradiated materials.* Ultramicroscopy, 111(2011), pp. 672-675.

[68] Y. Zhang, I.T. Bae, K. Sun, C. Wang, M. Ishimaru, Z. Zhu, W. Jiang, and W.J. Weber. *Damage profile and ion distribution of slow heavy ions in compounds.* Journal of Applied Physics, 105(2009), pp. 104901-12.

[69] F.Q. Yang. *Interaction between diffusion and chemical stresses.* Materials Science and Engineering: A, 409(2005), pp. 153-159.

[70] F.Q. Yang, K. Geng, P.K. Liaw, G.J. Fan, and H. Choo. *Deformation in a*

$Zr_{57}Ti_5Cu_{20}Ni_8Al_{10}$ bulk metallic glass during nanoindentation. Acta Materialia, 55(2007), pp. 321-327.

[71] D.C.C. Lam, and A.C.M. Chong. *Model and experiments on strain gradient hardening in metallic glass.* Materials Science and Engineering: A, 318(2001), pp. 313-319.

[72] C.A. Schuh, and T.G. Nieh. *A survey of instrumented indentation studies on metallic glasses.* Journal of Materials Research, 19(2004), pp. 46-57.

[73] F.Q.Yang, L.L.Peng, and K.J.Okazaki. *Micro-indentation of aluminum processed by equal channel angular extrusion.* Metallurgical and Materials Transactions A, 35(2004), pp.1243-1248.

[74] Y.T. Cheng, and C.M. Cheng. *Scaling relationships in conical indentation of elastic-perfectly plastic solids.* International Journal of Solids and Structures, 36 (1999), pp. 1231-1243.

[75] R. Vaidyanathan, M. Dao, G. Ravichandran and S. Suresh. *Interpretation of the Deformation Behavior of Bulk Metallic Glass through Multi-Scale Indentation.* Acta Materialia, 49 (2001), pp. 3781-3789.

[76] Y.T. Cheng, Z. Li, and C.M. Cheng. *Scaling relationships for indentation measurements.* Philosophical Magazine A, 82(2002), pp. 1821-1829.

[77] A. Flores, and F.J. Calleja. *Mechanical properties of poly(ethylene terephthalate) at the near surface from depth-sensing experiments.* Philosophical Magazine A, 78(1998), pp. 1283-1297.

[78] B.D. Beake, and G.J. Leggett. *Nanoindentation and nanoscratch testing of uniaxially and biaxially drawn poly(ethylene terephthalate) film.* Polymer, 43(2002), pp. 319-327.

[79] D.L. Joslin, and W.C. Oliver. *A new method for analyzing data from continuous depth-sensing microindentation tests.* Journal of

Materials Research, 5(1990), pp. 123-126.

[80] A.L. Greer, A. Castellero, S.V. Madge, I.T. Walker, and J.R. *Nanoindentation studies of shear banding in fully amorphous and partially devitrified metallic alloys.* Materials Science and Engineering: A, 375(2004), pp. 1182-1185.

[81] W.H. Jiang, G.J. Fan, F.X. Liu, G.Y. Wang, H. Choo, and P.K. Liaw. *Spatiotemporally inhomogeneous plastic flow of a bulk-metallic glass.* International Journal of Plasticity, 24(2008), pp. 1-16.

[82] H.Q. Li, K.X. Tao, C. Fan, H. Choo, and P.K. Liaw. *Effect of temperature on mechanical behavior of Zr-based bulk metallic glasses.* Applied Physics Letters, 89(2006), pp. 041921-3.

[83] L. Liu, and K.C. Chan. *Plastic deformation of Zr-based bulk metallic glasses under nanoindentation.* Materials Letters, 59(2005), pp. 3090-3094.

[84] P.M. Sargent, and M.F. Ashby. *Indentation creep*. Materials Science and Technology, 8(1992), pp. 594-601.

[85] H. Li, A.H.W. Ngan, and M.G. Wang. *Continuous Strain Bursts in Crystalline and Amorphous Metals During Plastic Deformation by Nanoindentation.* Journal of Materials Research, 20(2005), pp. 3072-3081.

[86] A. Gouldstone, H.-J. Koh, K.-Y. Zeng, A.E.Giannakopoulos, and S. Suresh. *Discrete and continuous deformation during nanoindentation of thin films.* Acta Materialia, 48(2000), pp. 2277-2295.

[87] T.G. Nieh, C. Schuha, J. Wadswortha, and Y. Li. *Strain rate-dependent deformation in bulk metallic glasses.* Intermetallics, 10 (2002), pp. 1177-1182.

[88] S. Guo, C. Ng, and C.T. Liu. *Anomalous solidification microstructures in Co-free $Al_xCrCuFeNi_2$ high-entropy alloys.* Journal of Alloys and Compounds, 557 (2013), pp. 77-81.

[89] C.W. Tsai, M.H. Tsai, J.W. Yeh, and C.C.Yang. *Effect of temperature on*

mechanical properties of $Al_{0.5}$CoCrCuFeNi wrought alloy. Journal of Alloys and Compounds, 490(2010), pp. 160-165.

[90] E.D. Tabachnikova, A.V. Podolskiy, S.N. Smirnov, I.A. Psaruk, V.Z. Bengus, H. Li, L. Li, H. Chu, and P.K. Liaw. *Thermal activation plasticity of nanocrystalline Ni-18.75 at.% Fe alloy in temperature range 4.2-350 K.* Low Temperature Physics. 38(2012), pp. 239-247.

[91] X. Yang, Y. Zhang, and P. K. Liaw. *Microstructure and com-pressive properties of NbTiVTaAl_x high entropy alloys.* Procedia Engineering, 36(2012), pp. 292-298.

[92] W.W. Gerberich, N.I. Tymiak, J.C. Grunlan. J Appl Mech. *Intepretation of indentation size effects.* Journal of Applied Mechanics, 69(2002), pp. 433-442.

[93] agilent.com; Available from: http://www.home.agilent.com.

Appendixes

Appendix A Tables

Table 1 Compositions and mechanical properties of ternary Zr-based bulk metallic glassy alloys. [43]

Element			Content, at%			σ_y	σ_f	E	HV
1	2	3	1	2	3				
Cu	Zr	Ag	50	45	5	—	1,940	112	599
Cu	Zr	Ag	50	45	5	—	1,940	112	599
Cu	Zr	Ag	45	47.5	7.5	—	1,820	108	556
Cu	Zr	Ag	45	45	10	—	1,810	108	542
Cu	Zr	Ag	42.5	47.5	10	—	1,780	106	534
Cu	Zr	Ag	45	50	5	—	1,885	111	585
Cu	Zr	Al	47.5	47.5	5	1,547	2,265	87	—
Cu	Zr	Al	55	40	5	—	2,210	115	581
Cu	Zr	Al	52.5	42.5	5	—	2,115	111	573
Cu	Zr	Al	50	45	5	—	1,885	102	546
Cu	Zr	Al	46	46	8	1,894	2,250	—	580
Cu	Zr	Al	55	40	5	—	2,210	115	581
Cu	Zr	Al	52.5	42.5	5	—	2,115	111	573
Cu	Zr	Al	50	45	5	—	1,885	102	546
Cu	Zr	Al	48	48	4	1,199	1,882	103	—
Cu	Zr	Al	47	47	6	1,733	2,250	—	580
Cu	Zr	Ga	52.5	42.5	5	—	1,940	105	552
Cu	Zr	Ga	55	40	5	—	2,025	109	565
Cu	Zr	Ga	52.5	40	7.5	—	2,130	111	581
Cu	Zr	Ga	57.5	40	2.5	—	1,910	105	547
Cu	Zr	Ti	60	30	10	1,785	2,150	114	—
Zr	Al	Ni	70	10	20	1,411	1,335	61	432
Zr	Al	Ni	65	10	25	1,581	1,520	64.5	484
Zr	Al	Ni	65	15	20	1,614	1,640	70.5	494
Zr	Al	Ni	60	15	25	1,640	1,715	72.6	502
Zr	Al	Ni	60	20	20	1,795	1,720	78.2	549
Zr	Co	Al	55	30	15	—	1,790	98	543

Table 1 Compositions and mechanical properties of ternary Zr-based bulk metallic glassy alloys. [43] Continued.

Element			Content, at%			σ_y	σ_f	E	HV
1	2	3	1	2	3				
Zr	Co	Al	55	25	20	—	1,750	96	530
Zr	Co	Al	55	25	20	—	1,900	114	—
Zr	Cu	Al	50	40	10	—	1,821	89	—
Zr	Cu	Al	50	40	10	—	1,860	88	496
Zr	Cu	Al	52.5	37.5	10	—	1,840	86	485
Zr	Cu	Al	50	37.5	12.5	—	1,960	93	511
Zr	Cu	Al	50	42.5	7.5	—	1,820	86	475
Zr	Cu	Al	55	35	10	—	1,810	83	470
Zr	Cu	Al	60	30	10	—	1,720	80	446
Zr	Cu	Al	47.5	42.5	10	—	1,920	90	508
Zr	Ni	Al	60	25	15	—	1,760	88	495
Zr	Ni	Al	55	25	20	—	1,780	89	502
Zr	Ni	Al	55	30	15	—	1,820	99	514
Zr	Ni	Al	60	20	20	1,793	1,720	78.2	549
Zr	Ni	Al	70	20	10	1,411	1,335	61	432
Zr	Ni	Al	65	25	10	1,520	1,581	64.5	484
Zr	Ni	Al	65	20	15	1,614	1,640	—	494
Zr	Ni	Al	60	25	15	1,640	1,715	—	502
Zr	Ni	Ti	40	37	23	—	1,630	—	524

Table 2 Compositions and mechanical properties of quaternary Zr-based bulk metallic glassy alloys. [43]

Element				Content, at%				σ_y	σ_f	E	HV
1	2	3	4	1	2	3	4				
Cu	Zr	Ag	Al	45	45	7	3	—	1,836	110	540
Cu	Zr	Ag	Al	45	45	5	5	—	1,890	112	556
Cu	Zr	Ag	Al	45	45	3	7	—	1,912	112	561
Cu	Zr	Hf	Ag	45	25	20	10	—	2,000	122	579
Cu	Zr	Ti	Be	55.5	27.75	9.25	7.5	—	2,450	146	710
Cu	Zr	Ti	Y	58.8	29.4	9.8	2	1,780	2,050	115	—
Ni	Nb	Ti	Zr	60	15	10	15	—	2,770	156	—
Ni	Ta	Ti	Zr	60	15	15	10	—	3,180	67	—
Zr	Al	Co	Cu	55	20	20	5	2,000	1,960	92	—
Zr	Al	Ni	Pd	65	7.5	10	17.5	1,340	1,510	—	—
Zr	Cu	Ni	Al	52	32	4	12	—	1,780	88	501
Zr	Cu	Ni	Al	52	30	6	12	—	1,820	93	506
Zr	Cu	Ni	Al	50	26	12	12	—	1,878	88	498
Zr	Cu	Ni	Al	50	34	4	12	—	1,905	91	517
Zr	Cu	Ni	Al	48	32	8	12	—	1,894	94	513
Zr	Cu	Ni	Al	50	32	6	12	—	1,875	92	521
Zr	Cu	Ni	Al	52	28	8	12	—	1,798	94	512
Zr	Cu	Ni	Al	50	30	8	12	—	1,820	92	526
Zr	Cu	Ni	Al	46	34	8	12	—	1,777	111	562
Zr	Cu	Ni	Al	48	28	12	12	—	1,906	102	530
Zr	Cu	Ni	Al	48	34	6	12	—	1,899	94	529
Zr	Cu	Ni	Al	50	28	10	12	—	1,993	92	517
Zr	Cu	Ni	Al	48	30	10	12	—	1,378	94	520
Zr	Cu	Ni	Al	48	30	10	12	—	1,980	92	528
Zr	Cu	Ni	Al	52	26	10	12	—	1,960	89	509
Zr	Cu	Ni	Al	46	30	12	12	—	1,399	106	552
Zr	Cu	Fe	Al	60	25	5	10	1,643	—	92	—
Zr	Cu	Fe	Al	60	20	10	10	1,708	—	104	—
Zr	Fe	Al	Cu	60	10	7.5	22.5	1,718	—	100	—

Table 3 Element of concentrations in different points and nominal element of concentration

	Al (at-%)	Cr (at-%)	Cu (at-%)	Fe (at-%)	Ni (at-%)
A	11.22	7.93	55.41	5.79	19.65
B	12.22	7.02	51.20	6.12	23.44
C	9.03	19.41	15.10	18.44	38.02
D	7.57	20.67	12.91	21.21	37.64
E	6.38	20.95	12.19	22.23	38.25
Nominal Concentration	9.1	18.2	18.2	18.2	36.4

Table 4 Irradiation parameters and peak positions predicted by SRIM under Au irradiation conditions.

Ion	Au
Ion energy (MeV)	10
Irradiation angle (°)	0
Irradiation area (mm^2)	100
Ion current (nA)	500
Irradiation time (hour)	10
Ion fluence (cm^{-2})	2.0×10^{16}
SRIM Au peak (nm)	1,130
SRIM dpa peak (nm)	900

Appendix B Figures

Indenting Tips Summary

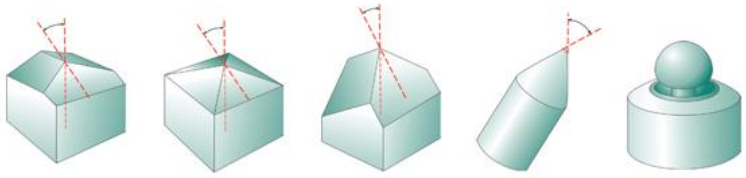

	Berkovich	Vickers	Cube-Corner	Cone (angle ψ)	Sphere (radius R)
Features					
Shape	3-sided pyramid	4-sided pyramid	3-sided pyramid w/ perpendicular faces	Conical	Spherical
Applications	Bulk Materials, Thin Films, Polymers, Scratch Testing, Wear Testing, MEMS, Imaging	Bulk Materials, Films and Foils, Scratch Testing, Wear Testing	Thin Films, Scratch Testing, Fracture Toughness, Wear Testing, MEMS, Imaging	Modeling, Scratch Testing, Wear Testing, Imaging, MEMS	MEMS
Available as Traceable Standard	Yes	Yes	Yes	No	No
Parameter					
Centerline-to-face angle, α A	65.3°	68°	35.2644°	—	—
Area (projected), A(d)	$24.56d^2$	$24.504d^2$	$2.5981d^2$	πa^2	πa^2
Volume-depth relation, V(d)	$8.1873d^3$	$8.1681d^3$	$0.8657d^3$	—	—
Projected area/face area, A/A_f	0.908	0.927	0.5774	—	—
Equivalent cone angle, ψ	70.32°	70.2996°	42.28°	ψ	—
Contact radius, a	—	—	—	d tan ψ	$(2Rd\text{-}d^2)^{1/2}$

Figure 1 Summary indentation-tip configurations [93]

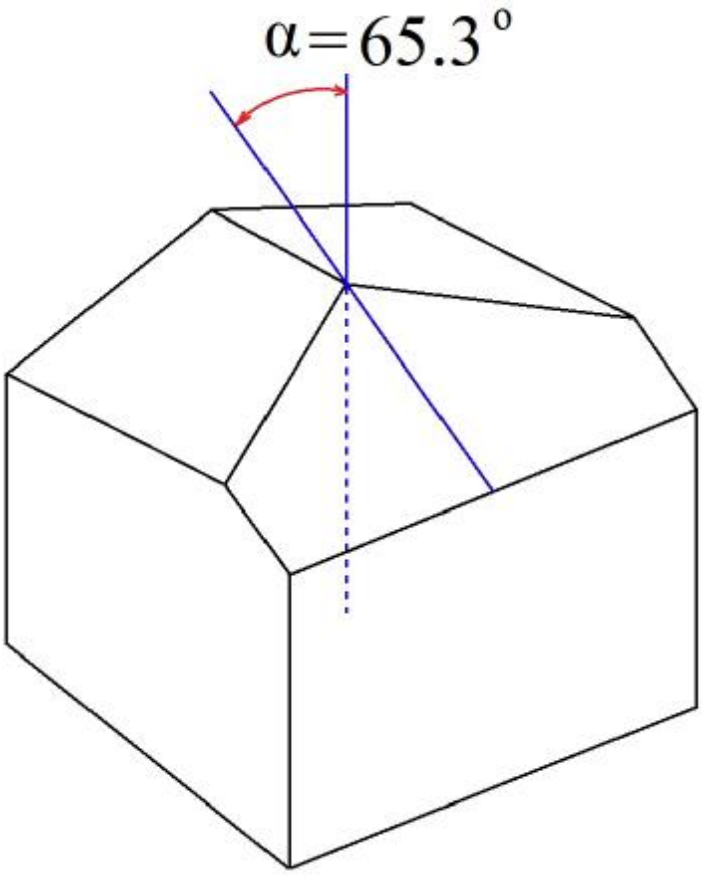

Figure 2 Berkovich indenter

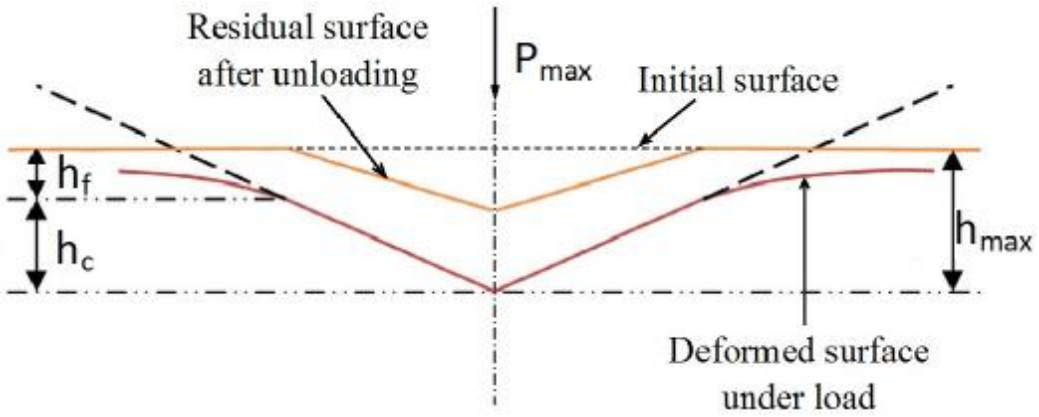

Figure 3 Nanoindentation loading and unloading

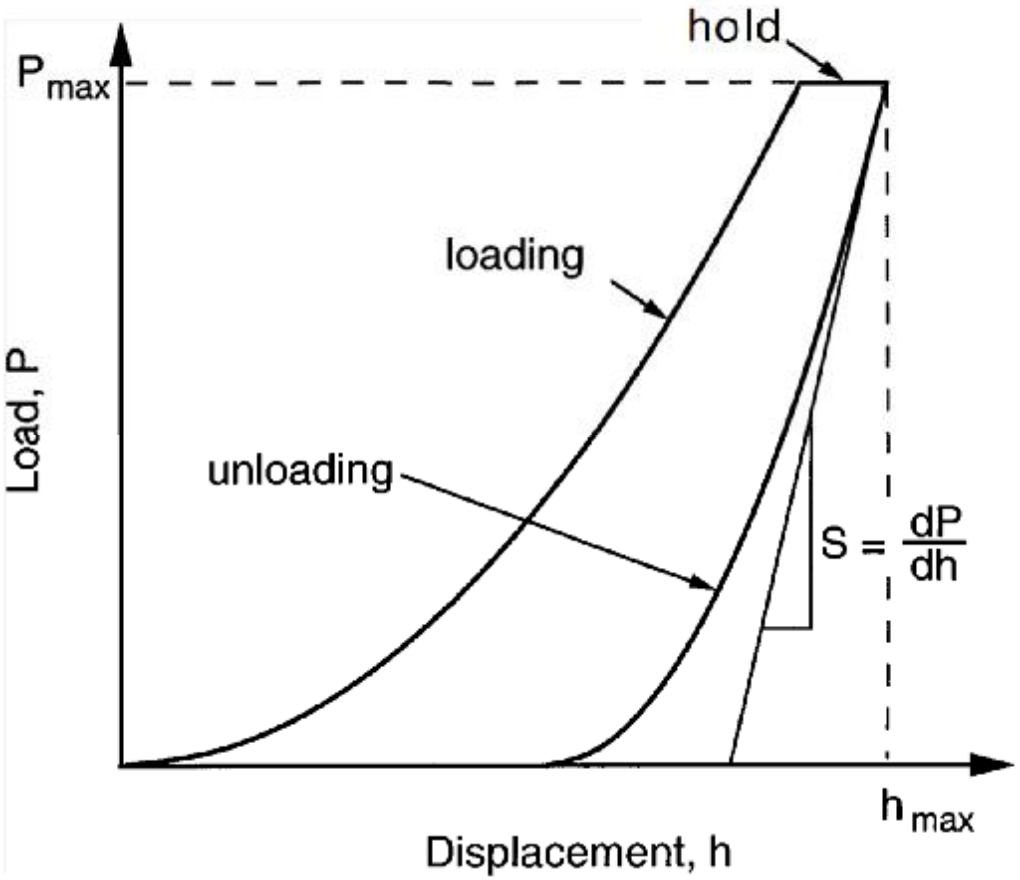

Figure 4 Schematic plot of a typical load-displacement curve.

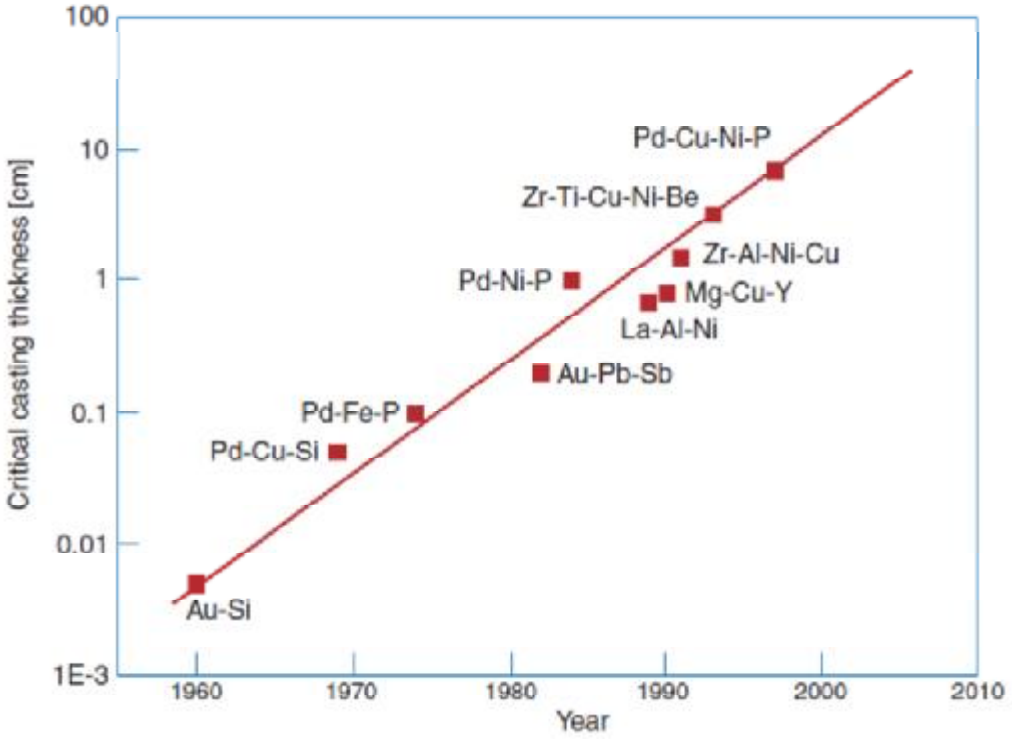

Figure 5 Critical casting thicknesses for glass formation as a function of the year the corresponding alloy has been discovered. Over 40 years, the critical casting thickness has increased by more than three orders of magnitude. [25]

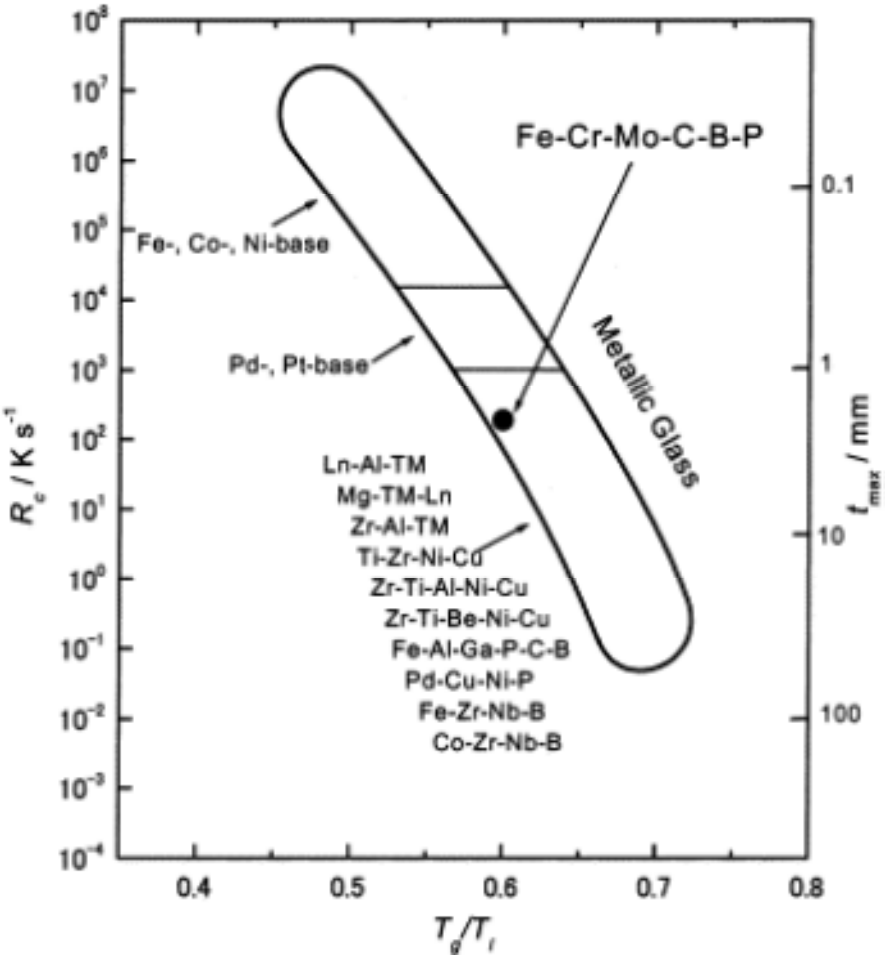

Figure 6 Relation among the critical cooling rate for glass formation (R_c), maximum thickness for glass formation (t_{max}), and reduced glass-transition temperature (T_g/T_l) for metallic glasses. [29]

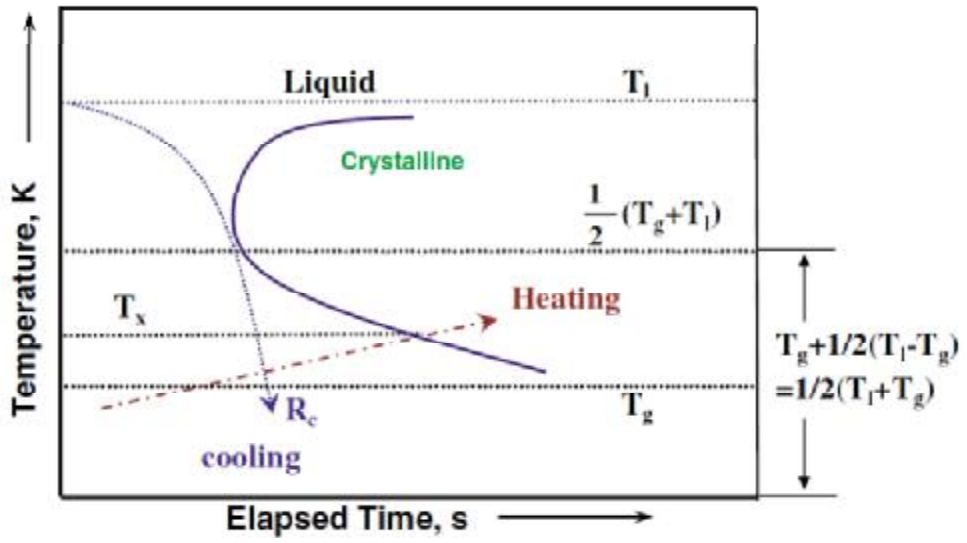

Figure 7 Schematic time-temperaturetransformation (TTT) diagram. Crystallization occurs between T_l and T_g, and can be avoided by sufficiently cooling of the liquid (R_c); when the amorphous solids are isochronally heated at a constant heating rate, the sample starts to crystallize at an onset temperature denoted as T_x. [36]

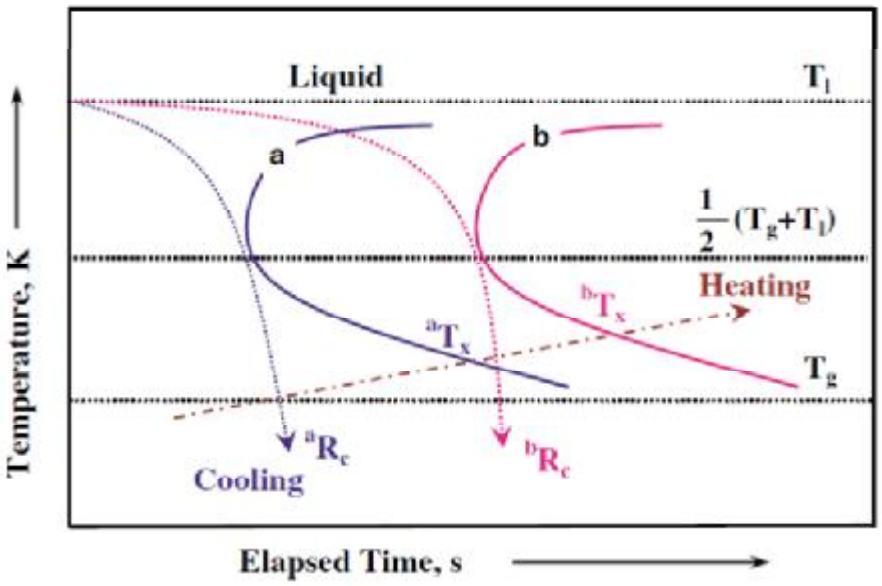

Figure 8 Schematic TTT curves showing the effect of T_x measured upon continuous heating for different liquids with similar T_l and T_g; liquid b with higher onset crystallization temperature bTx ($aT_x < bT_x$) shows a lower critical cooling rate bR_c ($bR_c < aR_c$). [36]

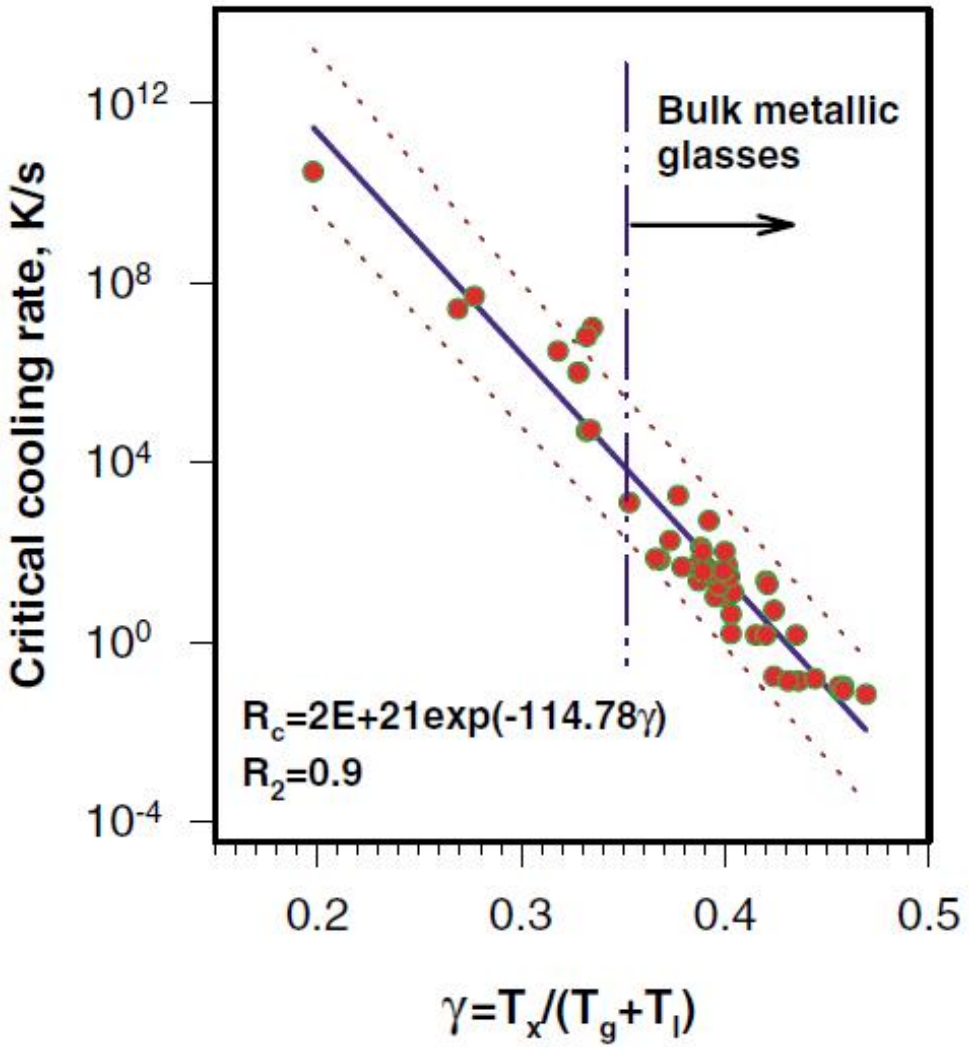

Figure 9 The correlation between the critical cooling rate and the parameter γ for 49 metallic glasses. [36]

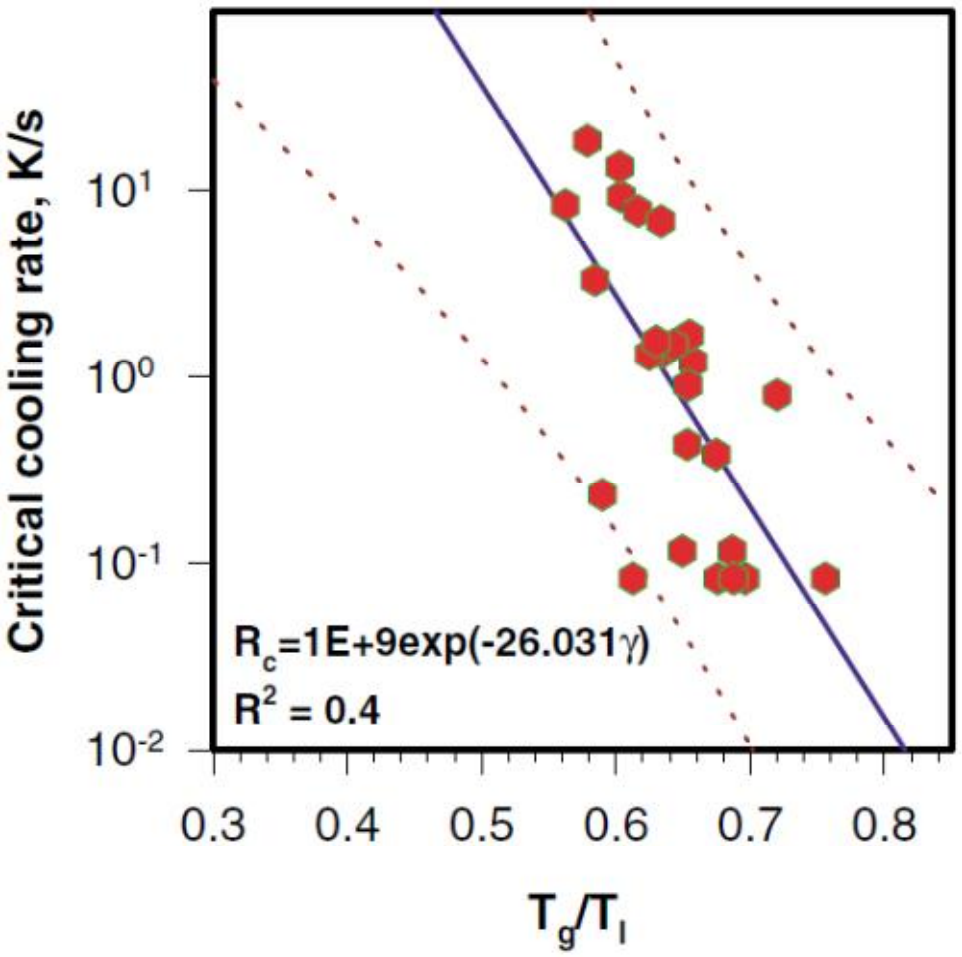

Figure 10 The critical cooling rates as a function of the reduced glass transition temperature T_{rg} for cryoprotective agents. [36]

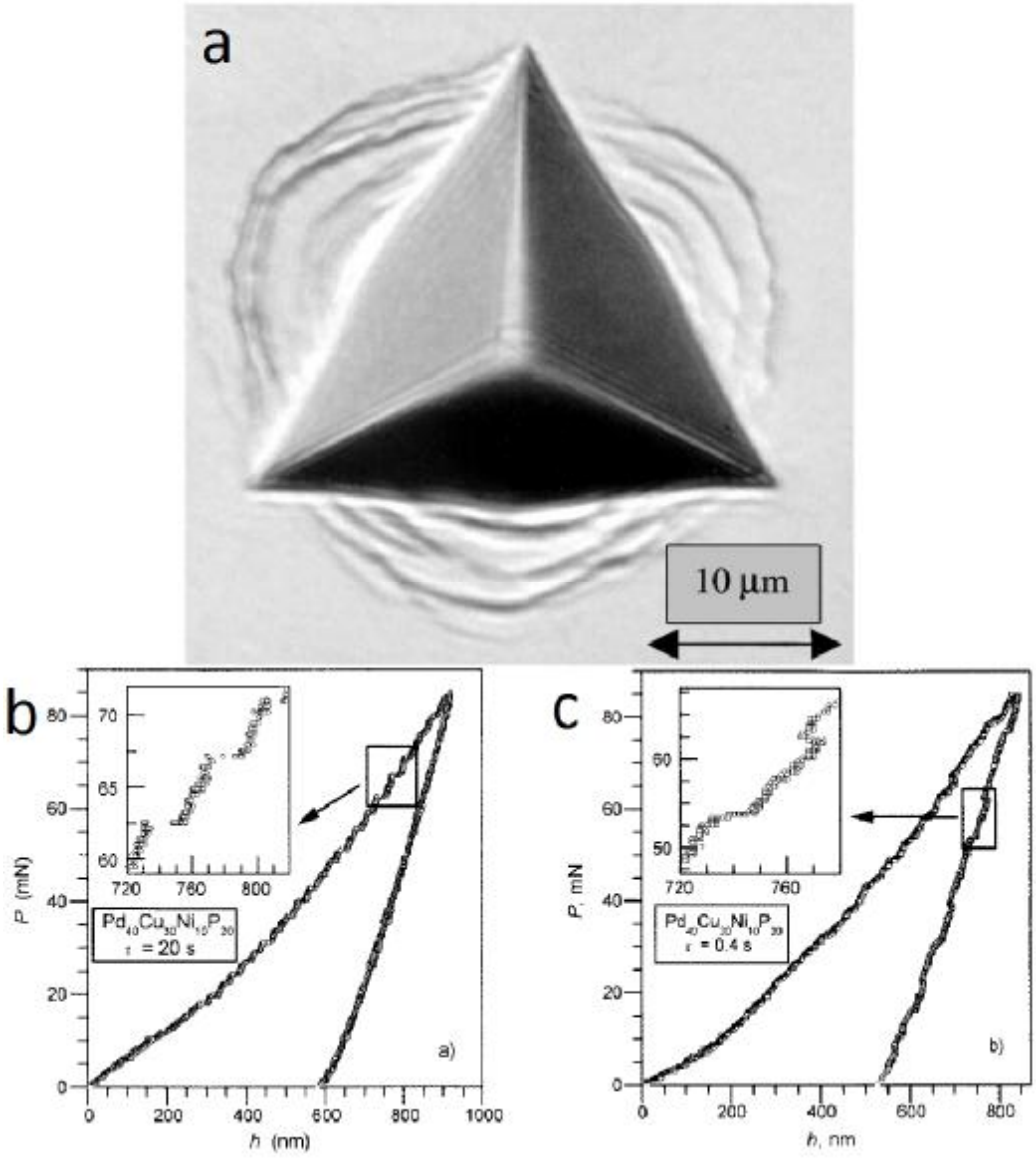

Figure 11 Localized plastic flow around a Berkovich indent on the surface of bulk amorphous $Pd_{40}Cu_{30}Ni_{10}P_{20}$. Indentation diagrams obtained by action of symmetric triangle force pulses with the duration of 20s (b) and 0.5s (c). The insets show the parts of the diagrams on an enlarged scale. [51]

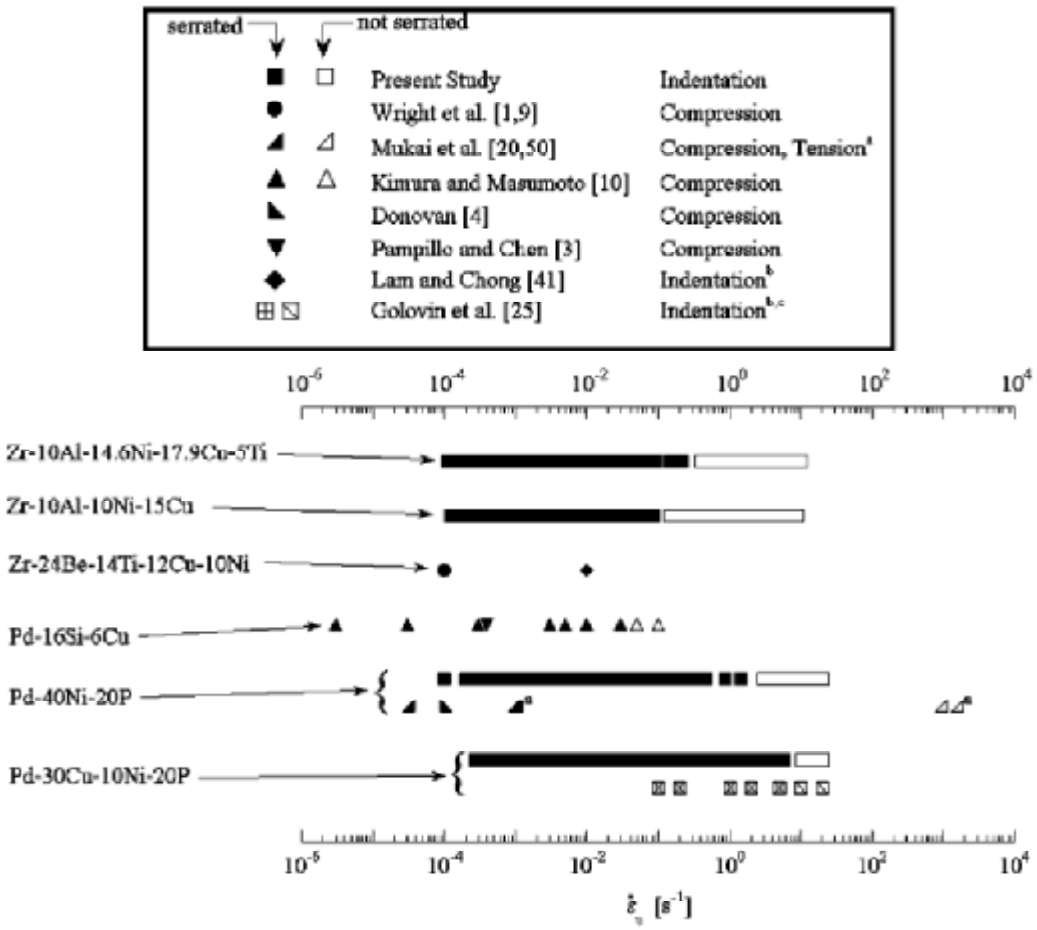

Figure 12 Compilation of the present indentation results, showing the range of strain rates over which serrated flow is and is not observed. Data from the literature are also assembled, illustrating the same general trends found in this work, in several different modes of loading. [44]

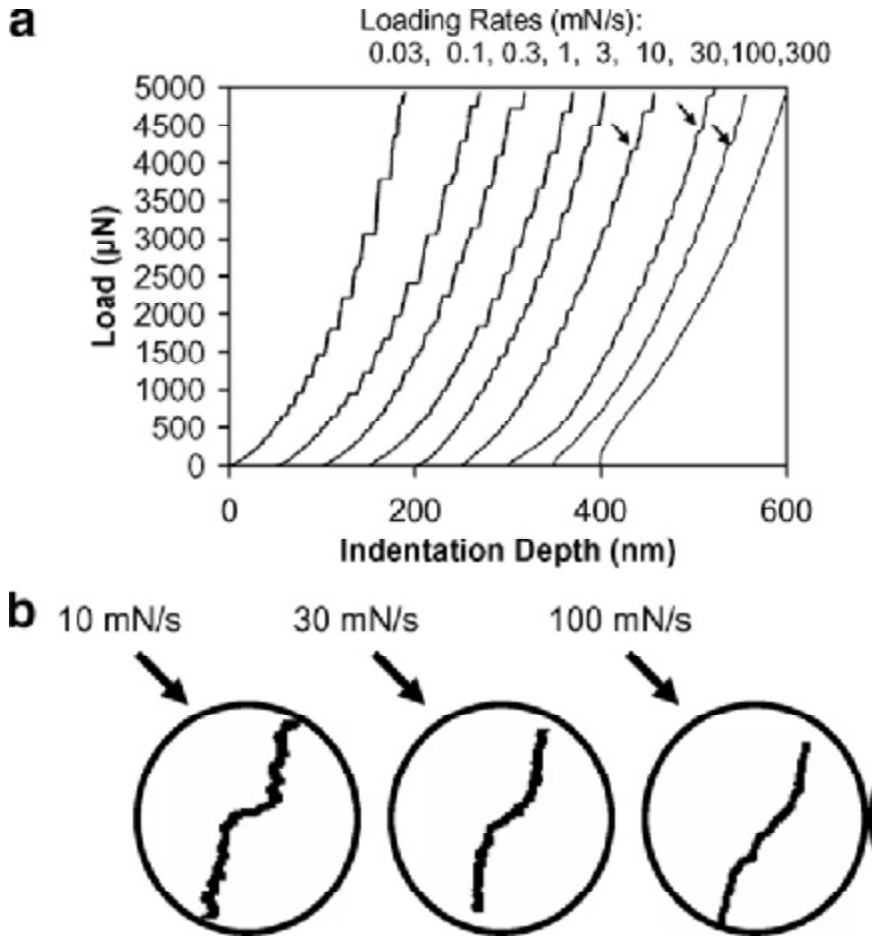

Figure 13 Pop-in size variation with the loading rates during nanoindentation of an Au-based bulk metallic glass. (a) *P-h* curves at nine different loading rates and (b) typical pop-in step at high loading rates of 10, 30, and 100 mNs^{-1}. [44]

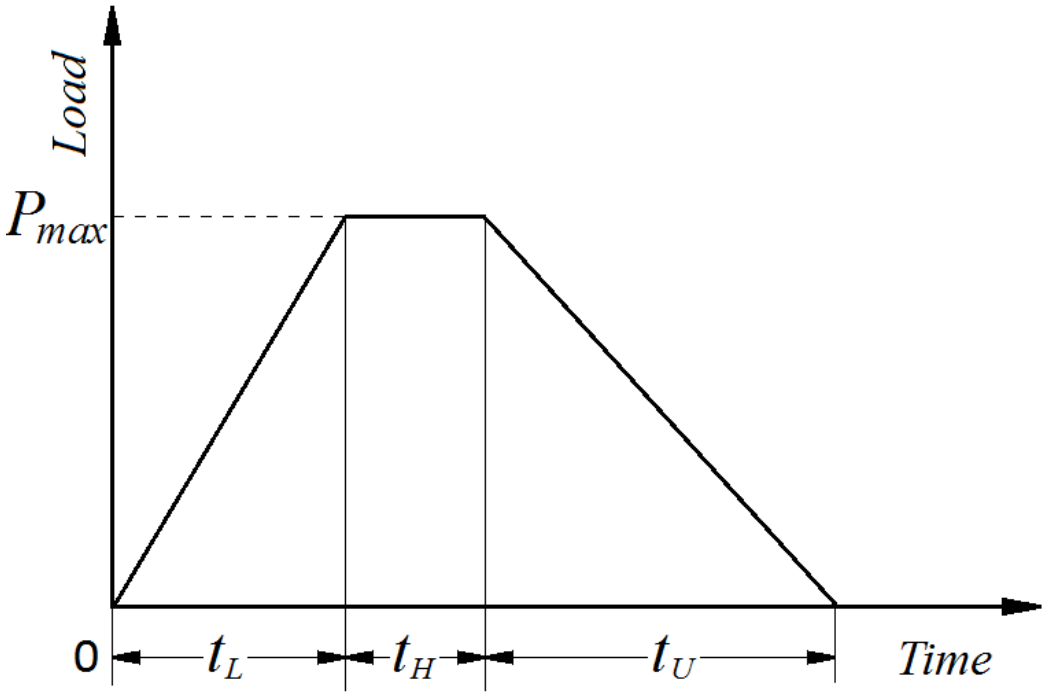

Figure 14 Sketch of the Indentation load versus time curve

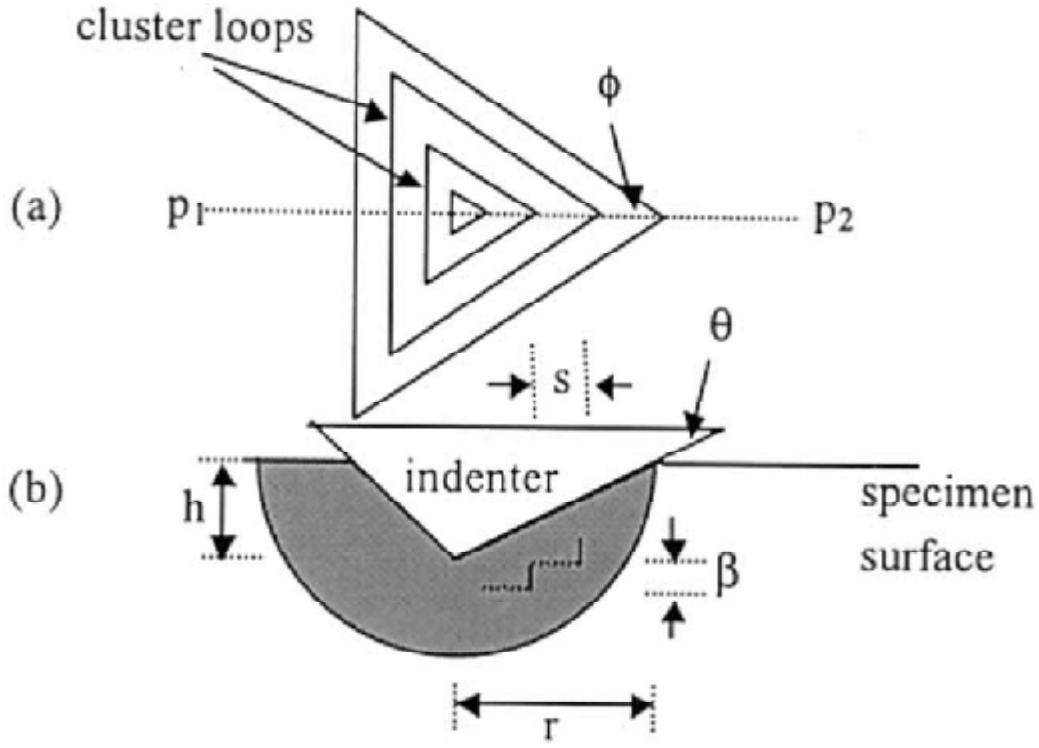

Figure 15 Schematic of the strain gradient clusters, (A) Top view of indentation impression, (B) Cross-sectional view along line *p1-p2*. [71]

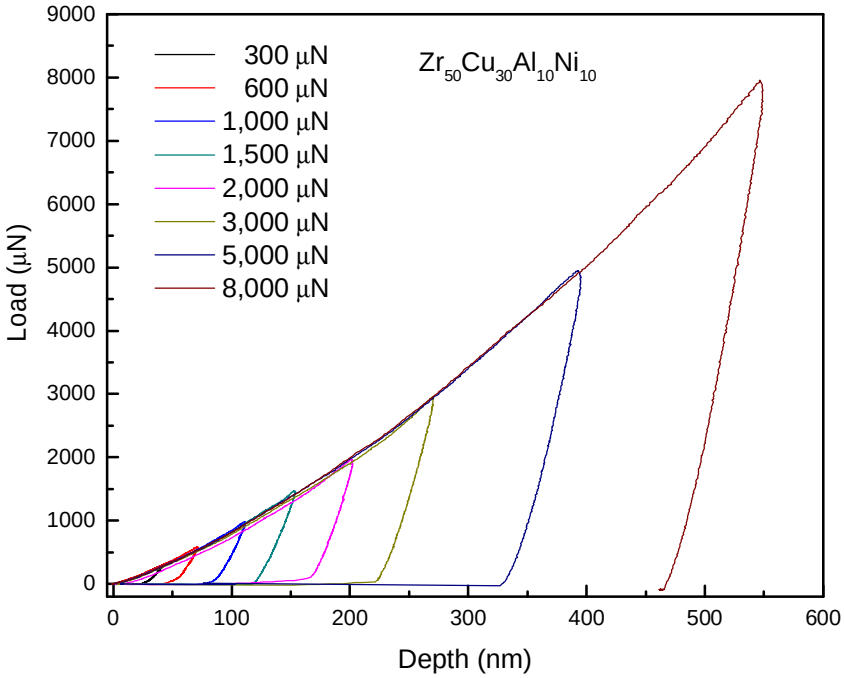

Figure 16 Load-Displacement curves of the $Zr_{50}Cu_{30}Al_{10}Ni_{10}$ BMGs at different indentation loading.

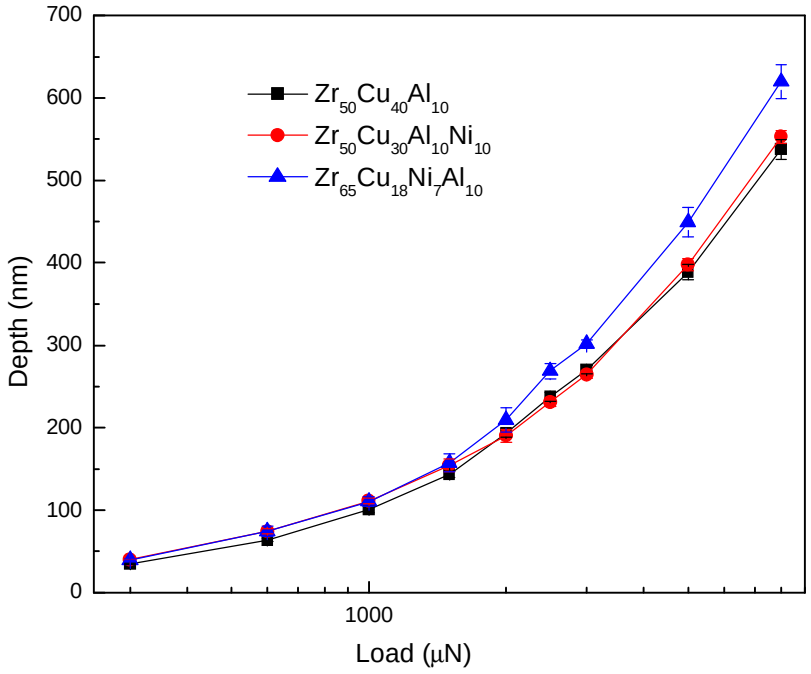

Figure 17 Dependence of the maximum indentation depth on the indentation load for the $Zr_{50}Cu_{40}Al_{10}$, $Zr_{50}Cu_{30}Al_{10}Ni_{10}$, and $Zr_{65}Cu_{18}Ni_7Al_{10}$ BMGs.

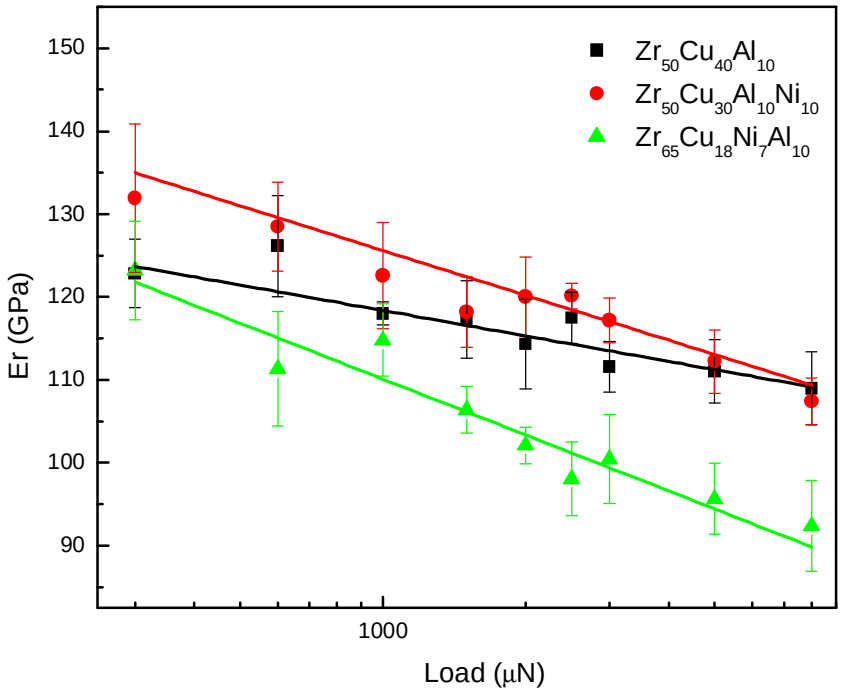

Figure 18 Effect of the indentation load on the reduced contact stiffness for the $Zr_{50}Cu_{40}Al_{10}$, $Zr_{50}Cu_{30}Al_{10}Ni_{10}$, and $Zr_{65}Cu_{18}Ni_7Al_{10}$ BMGs.

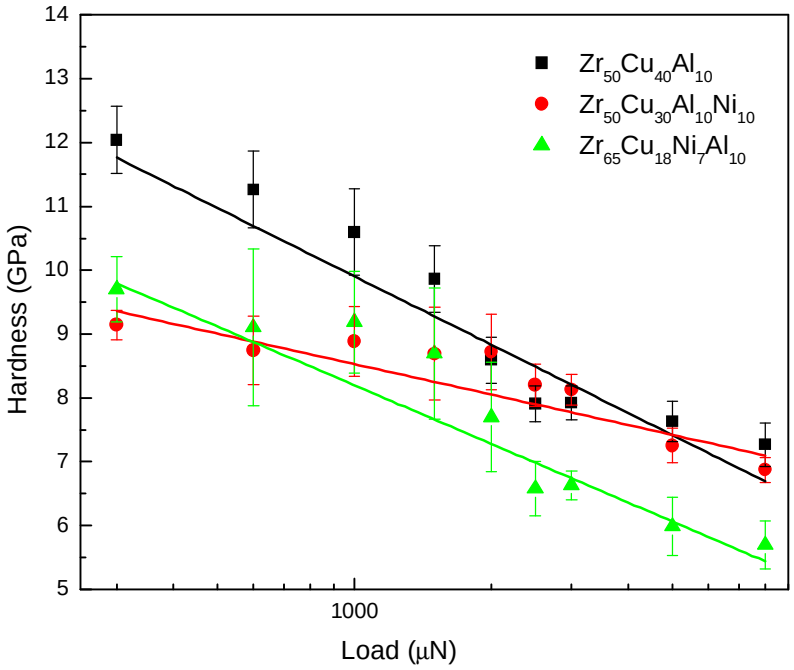

Figure 19 Dependence of the indentation hardness on the indentation load for the $Zr_{50}Cu_{40}Al_{10}$, $Zr_{50}Cu_{30}Al_{10}Ni_{10}$, and $Zr_{65}Cu_{18}Ni_7Al_{10}$ BMGs.

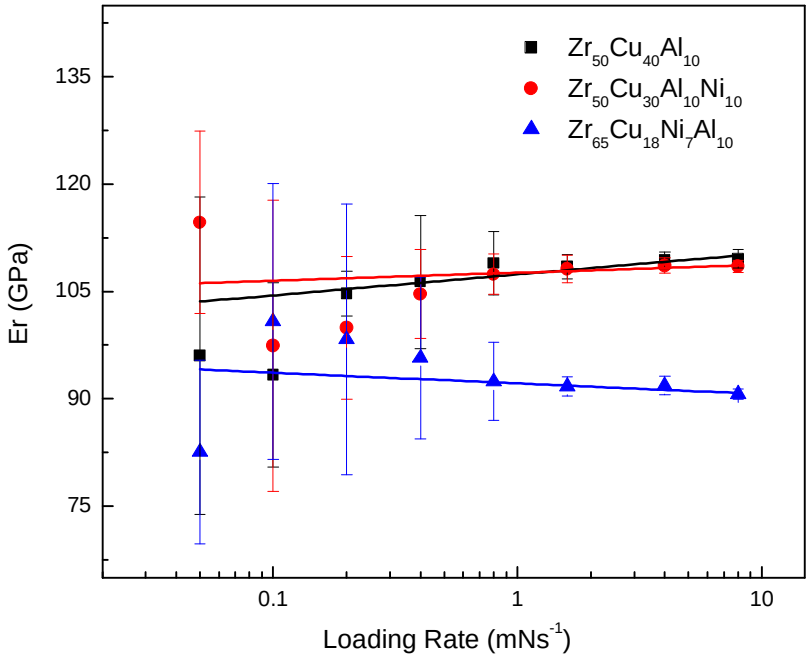

Figure 20 The reduced modulus (E_r) variation with the loading rate during nanoindentation of the $Zr_{50}Cu_{40}Al_{10}$, $Zr_{50}Cu_{30}Al_{10}Ni_{10}$, and $Zr_{65}Cu_{18}Ni_7Al_{10}$ BMGs.

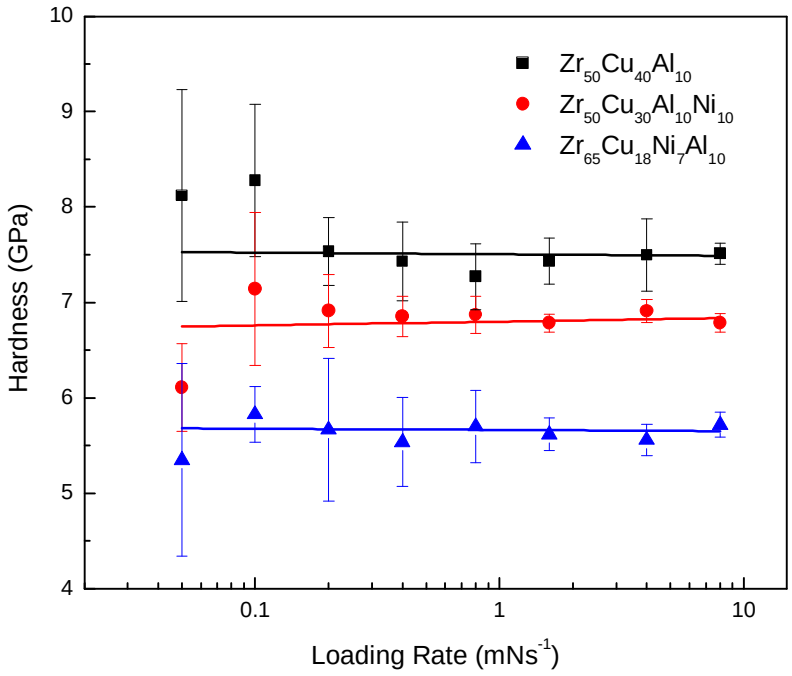

Figure 21 The hardness (*H*) variation with the loading rate during nanoindentation of the $Zr_{50}Cu_{40}Al_{10}$, $Zr_{50}Cu_{30}Al_{10}Ni_{10}$, and $Zr_{65}Cu_{18}Ni_7Al_{10}$ BMGs.

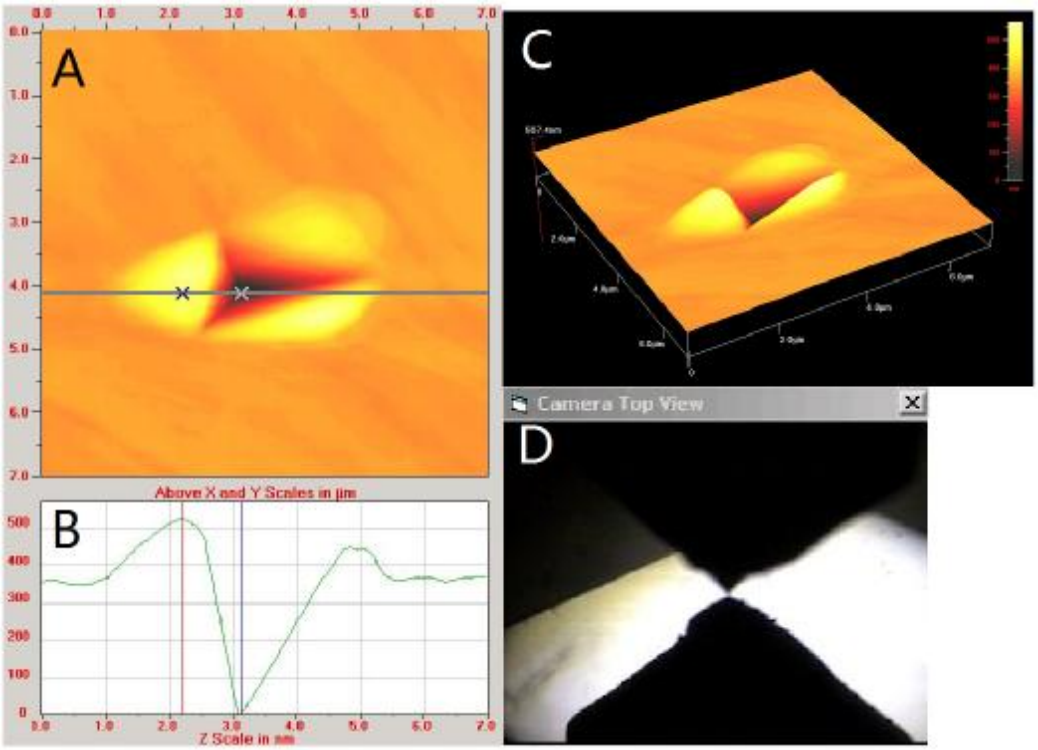

Figure 22 Slip-step patterns over the contact surface and the surrounding area of the $Zr_{50}Cu_{40}Al_{10}$ BMGs.

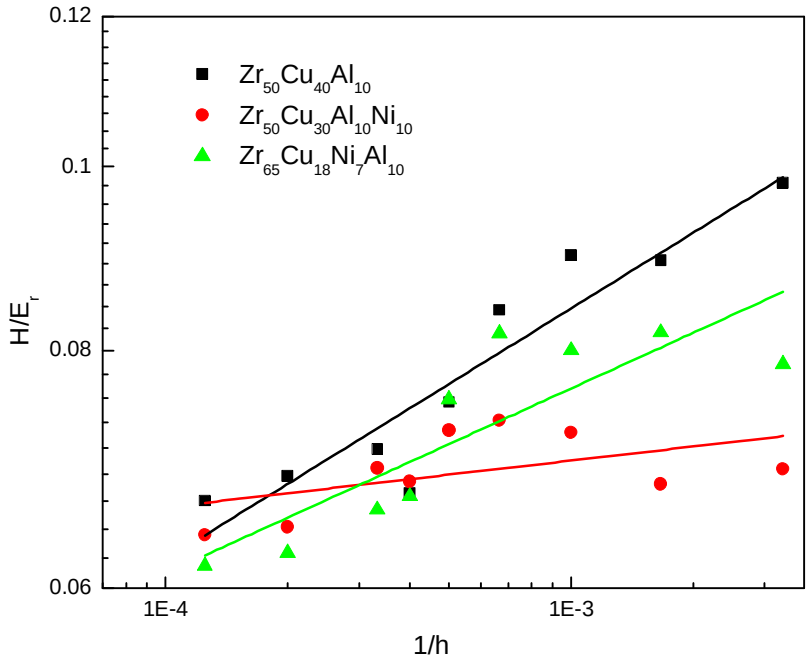

Figure 23 Indentation-size effects in the indentation of the $Zr_{50}Cu_{40}Al_{10}$, $Zr_{50}Cu_{30}Al_{10}Ni_{10}$, and $Zr_{65}Cu_{18}Ni_7Al_{10}$ BMGs.

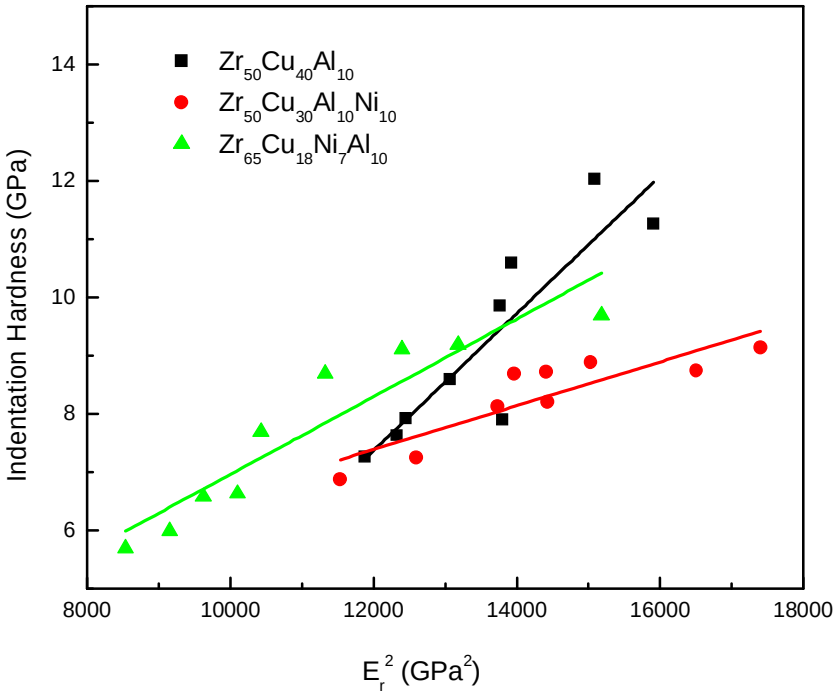

Figure 24 Correlation between the indentation hardness and the reduced contact modulus for the $Zr_{50}Cu_{40}Al_{10}$, $Zr_{50}Cu_{30}Al_{10}Ni_{10}$, and $Zr_{65}Cu_{18}Ni_7Al_{10}$ BMGs.

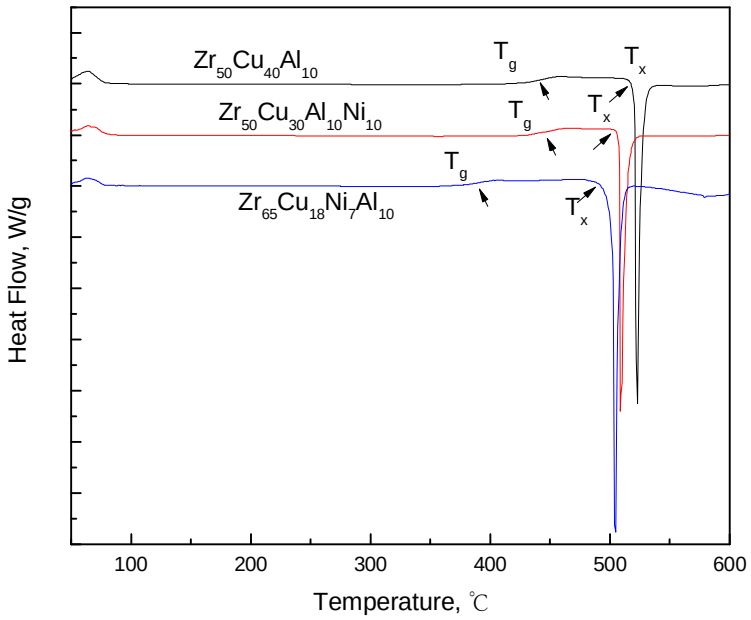

Figure 25 The temperature dependence of the DSC thermogram for the $Zr_{50}Cu_{40}Al_{10}$, $Zr_{50}Cu_{30}Al_{10}Ni_{10}$, and $Zr_{65}Cu_{18}Ni_7Al_{10}$ BMGs.

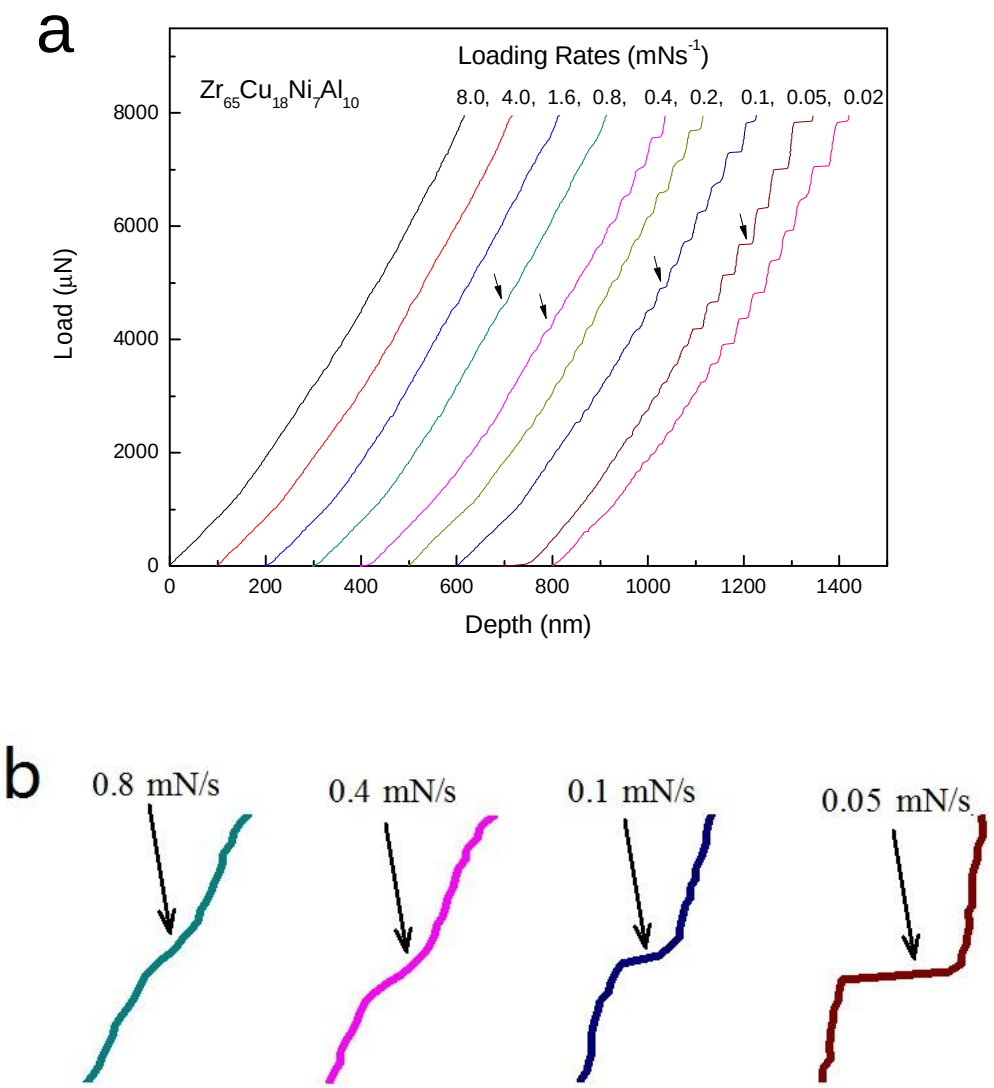

Figure 26 Pop-in size variations with the loading rates during nanoindentation of a $Zr_{65}Cu_{18}Ni_7Al_{10}$ BMG. (a) Typical load-displacement (*P-h*) for the loading portion of a nanoindentation test. (b) Typical pop-in gap at the loading rates of 0.8, 0.4, 0.1 and 0.05 mNs^{-1}.

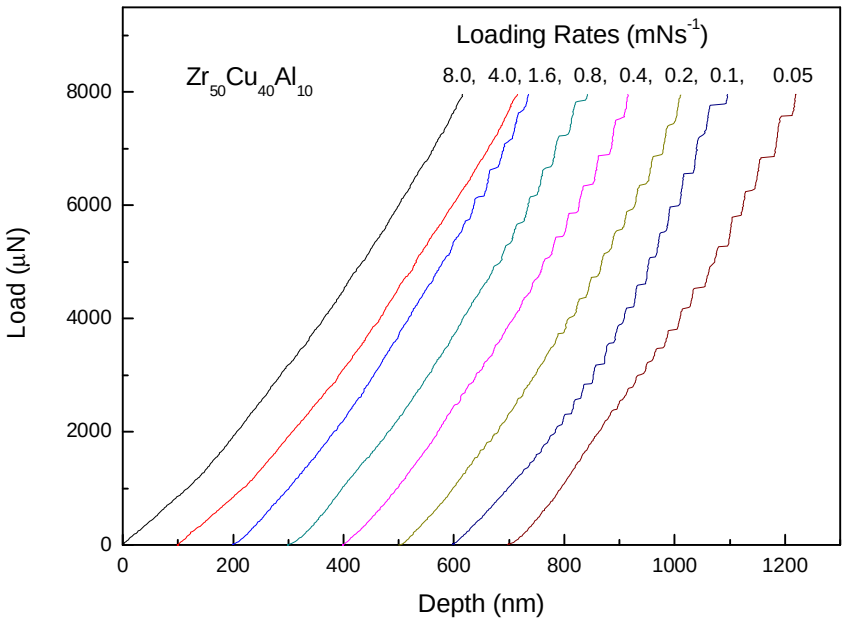

Figure 27 Typical load-displacement (*P*-*h*) for the loading portion of a nanoindentation test on a $Zr_{50}Cu_{40}Al_{10}$ BMG.

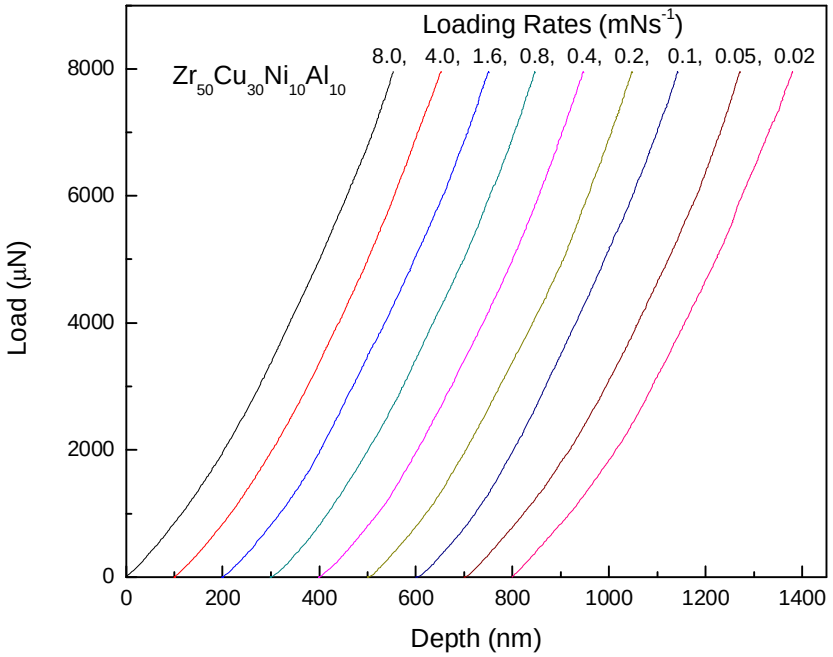

Figure 28 Typical load-displacement (*P*-*h*) for the loading portion of a nanoindentation test on a $Zr_{50}Cu_{30}Al_{10}Ni_{10}$ BMG.

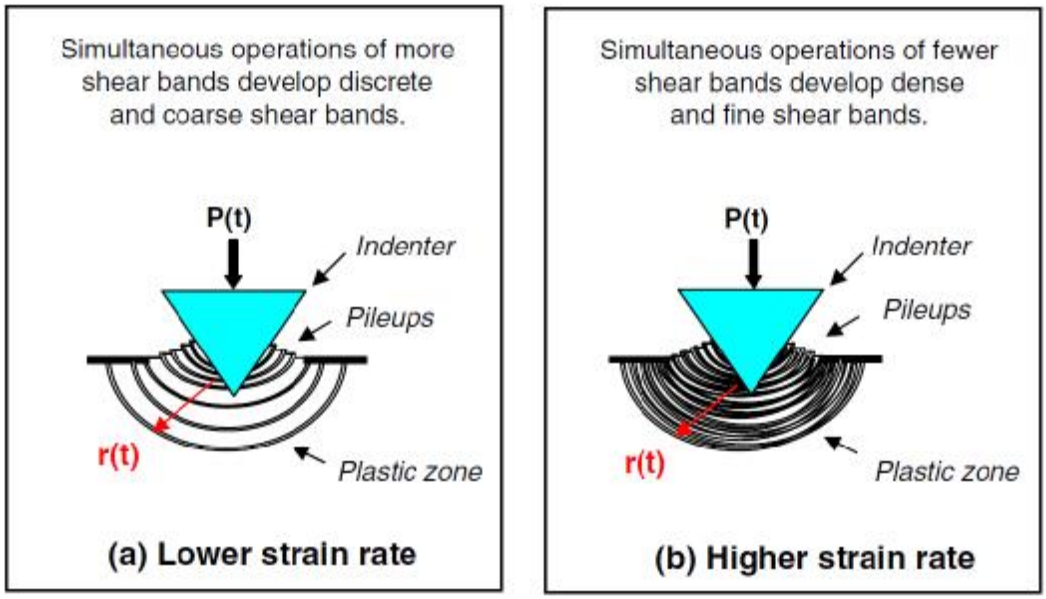

Figure 29 Schematic illustrations of cross-sectional views of the plastic deformation of a metallic glass during the nanoindentation at (a) a lower strain rate and (b) a higher strain rate. *P(t)* and *r(t)* represent the load and the plastic-zone size, respectively, both of which are a function of time. The shear-band patterns beneath the indents manifest the temporal characteristic features of shear-banding operations that we observed in the uniaxial compression. [81]

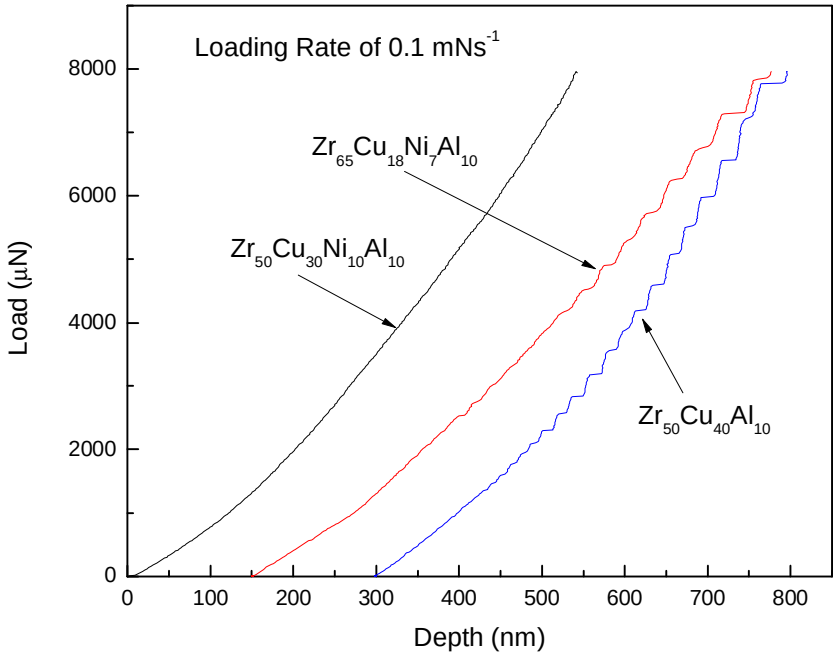

Figure 30 The typical *P-h* curves with the loading rate of 0.1 mNs^{-1} for $Zr_{50}Cu_{40}Al_{10}$, $Zr_{50}Cu_{30}Al_{10}Ni_{10}$ and $Zr_{65}Cu_{18}Ni_7Al_{10}$ BMGs.

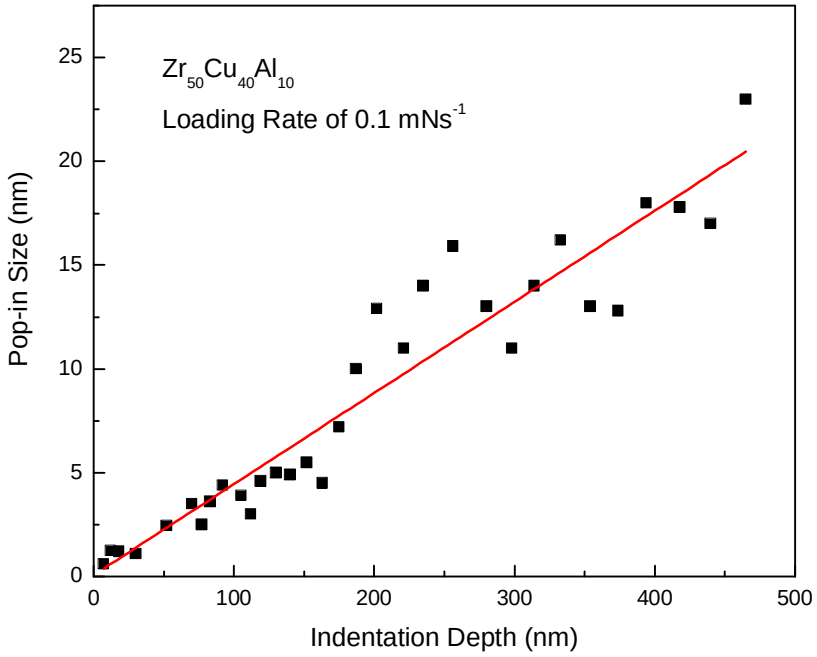

Figure 31 The function of measured pop-in size and the indentation depth for $Zr_{50}Cu_{40}Al_{10}$ BMGs indented at a constant loading rate of 0.1 mNs^{-1} during nanoindentation.

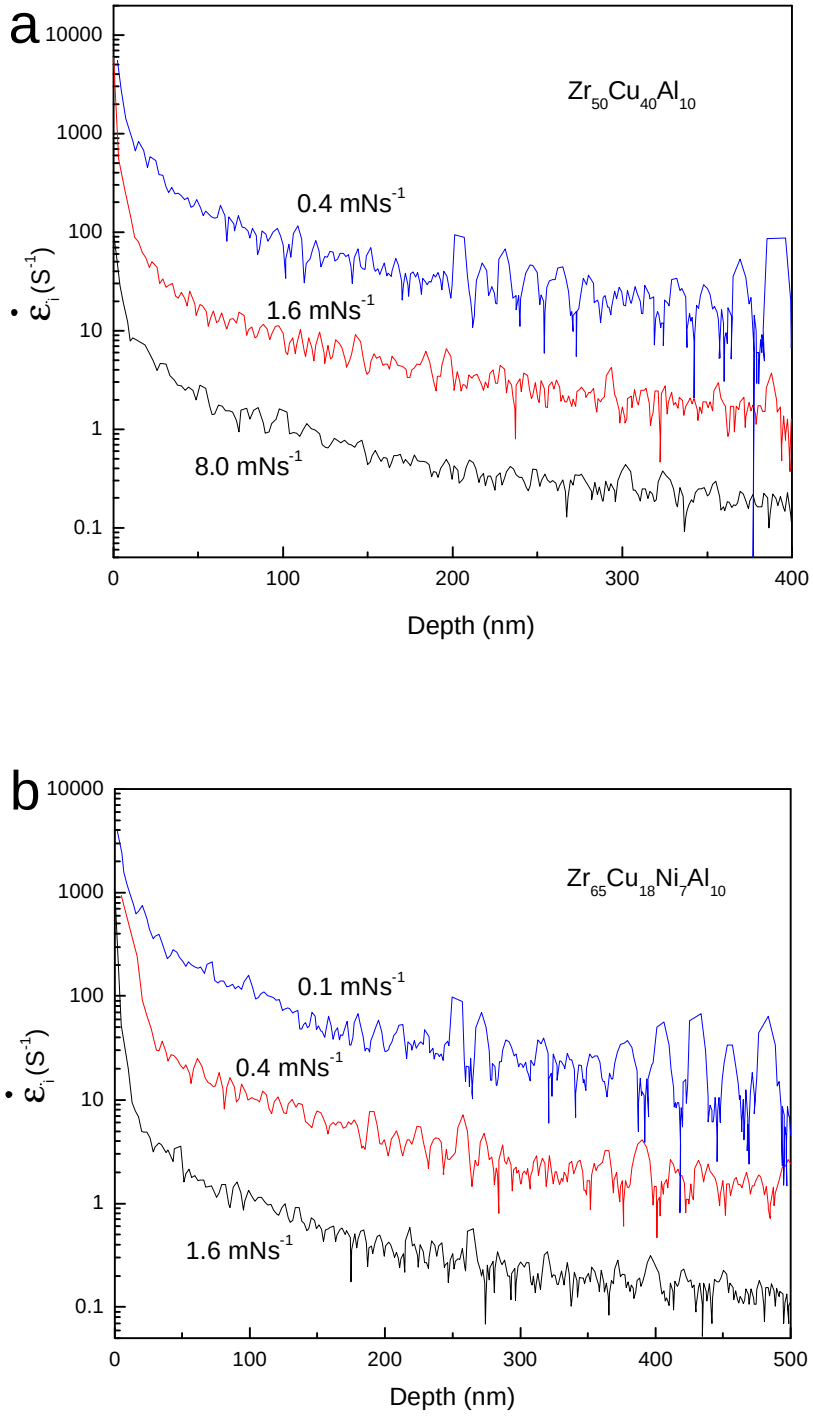

Figure 32 The indentation strain rate plotted as a function of the indentation depth for (a) $Zr_{50}Cu_{40}Al_{10}$ and (b) $Zr_{65}Cu_{18}Ni_7Al_{10}$BMGs at different loading rates.

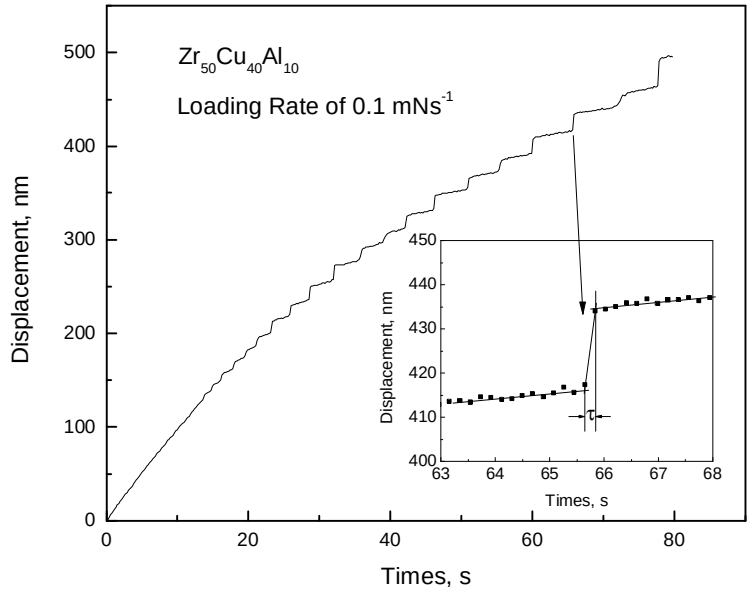

Figure 33 A typical curve of the indenter displacement vs. time (*h*-*t*) of the $Zr_{50}Cu_{40}Al_{10}$ BMGs at the loading rate of 0.1 mNs^{-1}.

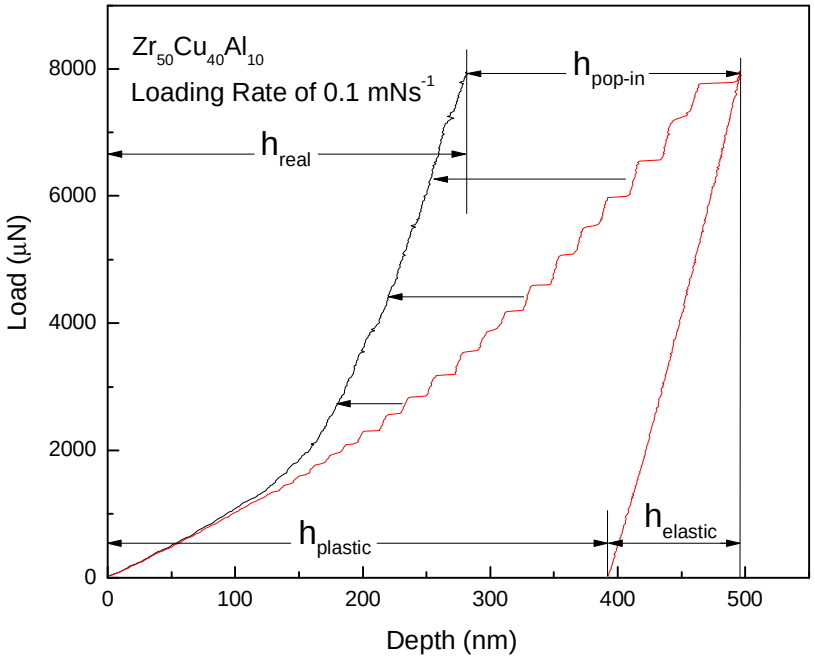

Figure 34 An example of a typical serrated *P-h* curve at a loading rate of 0.1 mNs^{-1} for the $Zr_{50}Cu_{40}Al_{10}$ BMGs, including the elastic-plastic loading and elastic unloading curve. As indicated by the arrows, a smooth "consolidated elastic" curve is obtained by removal of the pop-in gap.

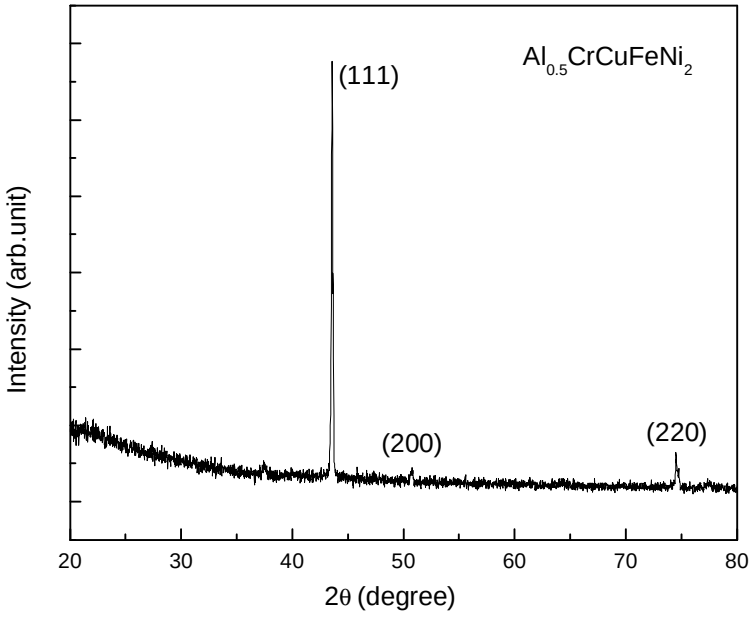

Figure 35 XRD patterns of as-cast $Al_{0.5}CrCuFeNi_2$ alloys. The structure of the as-cast and irradiated samples was performed by X-ray diffraction (XRD) with Cu Kα radiation (λ = 1.541874 Å).

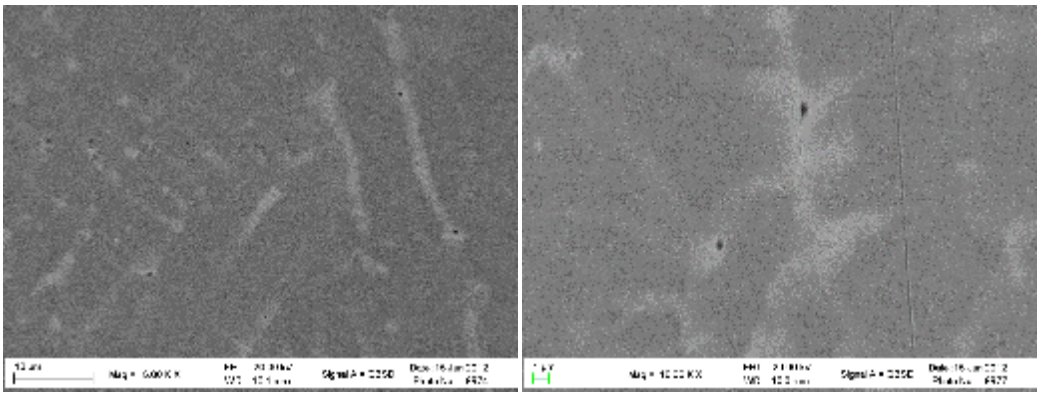

Figure 36 Scanning electron microscopy (SEM) image of the surface of the as-cast $Al_{0.5}CrCuFeNi_2$ HEA samples.

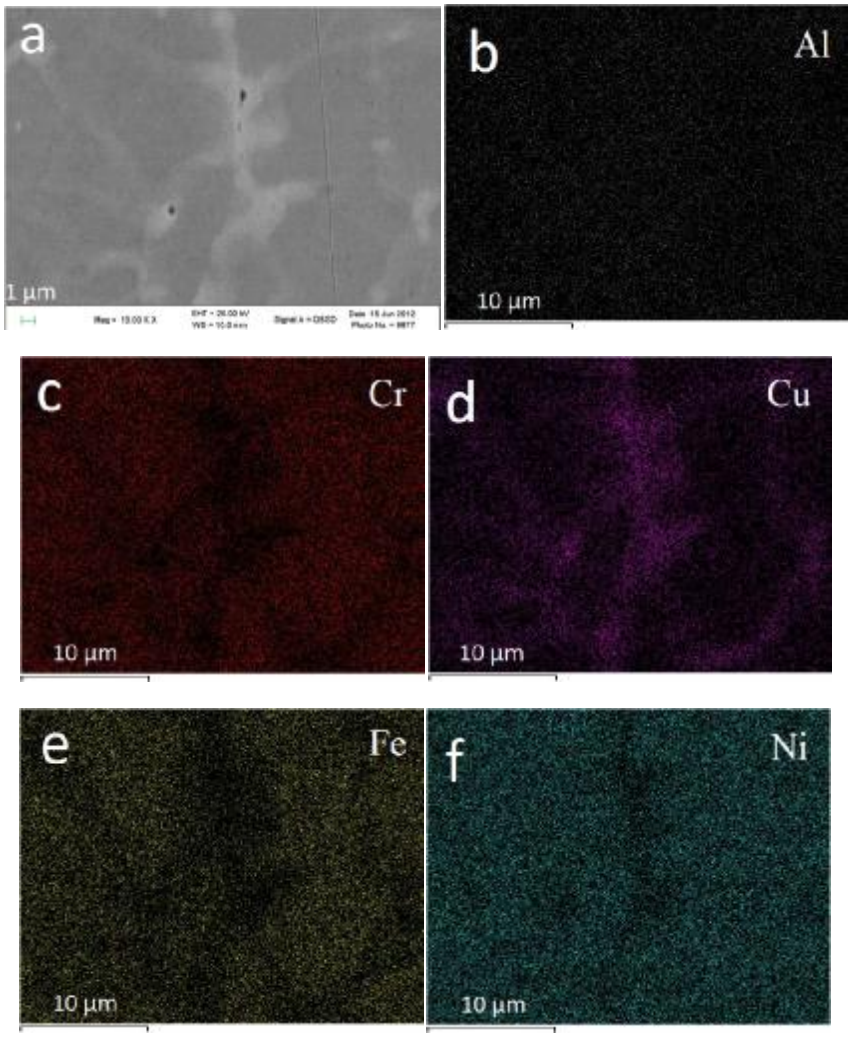

Figure 37 Elemental mapping of the $Al_{0.5}CrCuFeNi_2$ HEA.

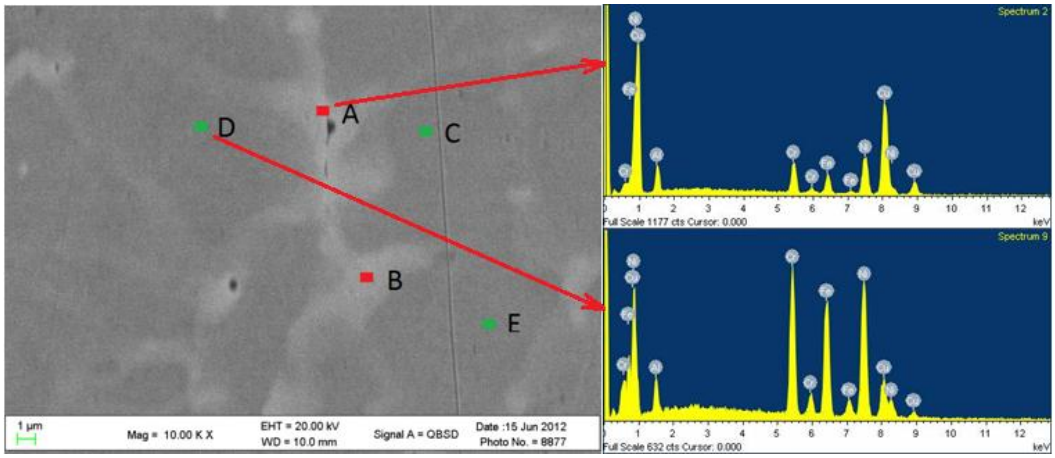

Figure 38 Surface elements analysis of the $Al_{0.5}CrCuFeNi_2$ HEA.

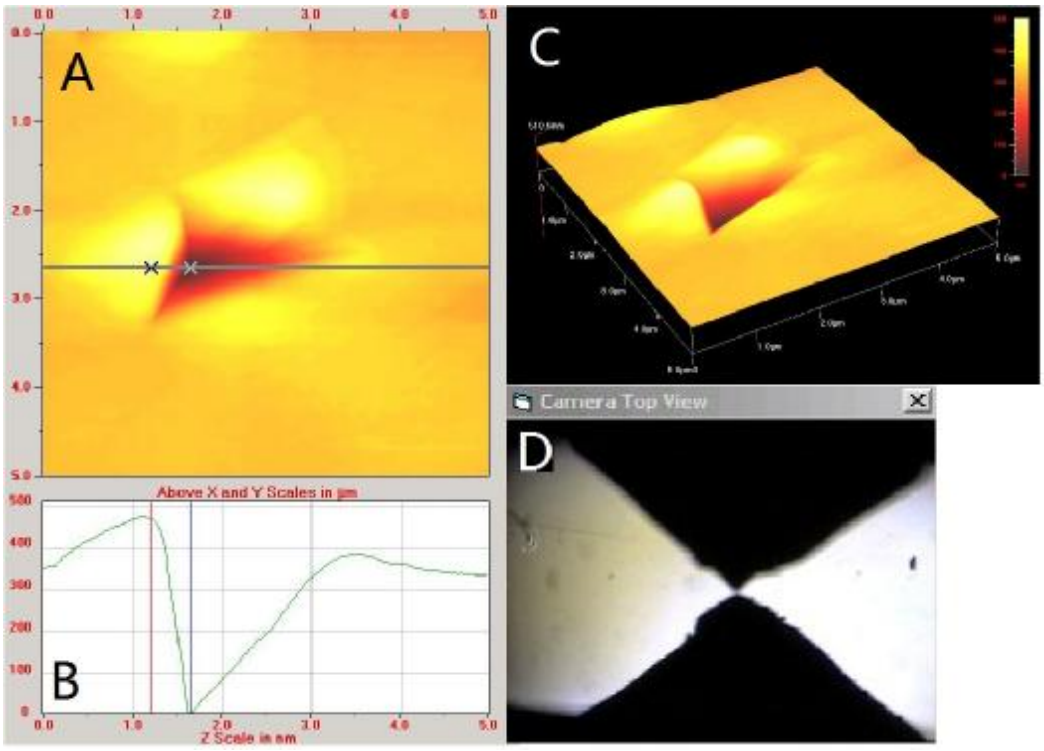

Figure 39 Slip-step patterns over the contact surface and the surrounding area of the $Al_{0.5}CrCuFeNi_2$ HEA

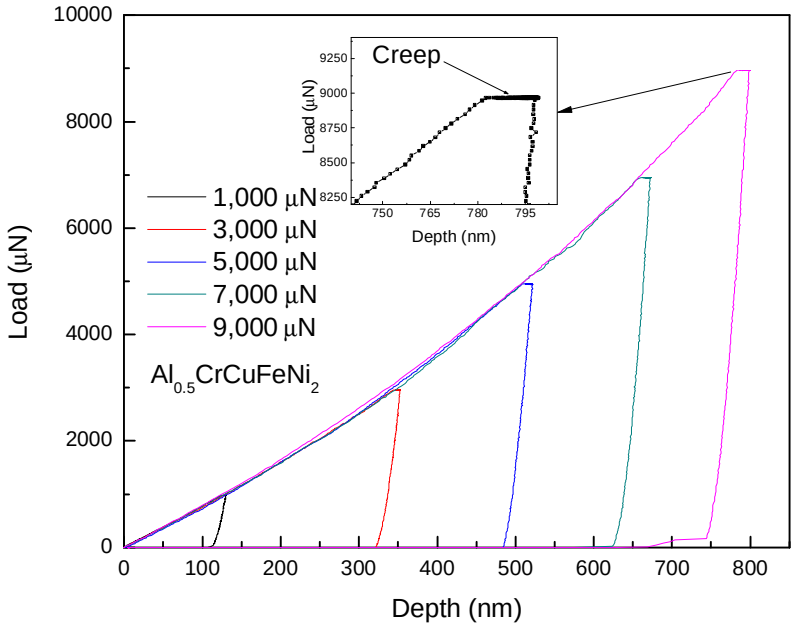

Figure 40 Load-displacement curves (*P-h*) as a function of normal load during nanoindentation of the $Al_{0.5}CrCuFeNi_2$ HEA.

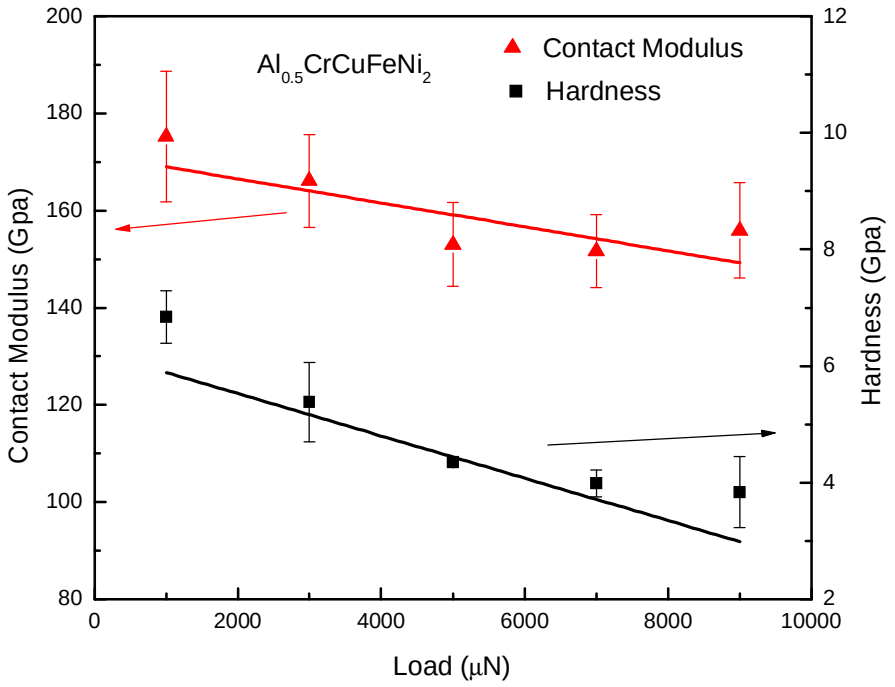

Figure 41 The reduced modulus (E_r) and hardness (H) variation with the value of load during nanoindentation of the $Al_{0.5}CrCuFeNi_2$ HEA.

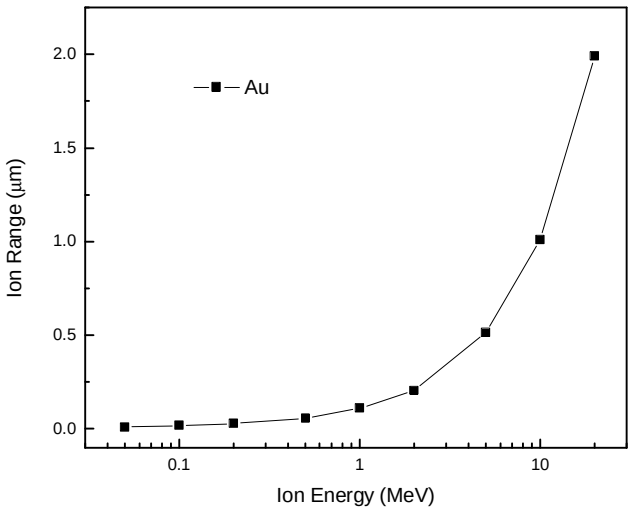

Figure 42 The relationship between ion energy and ion range

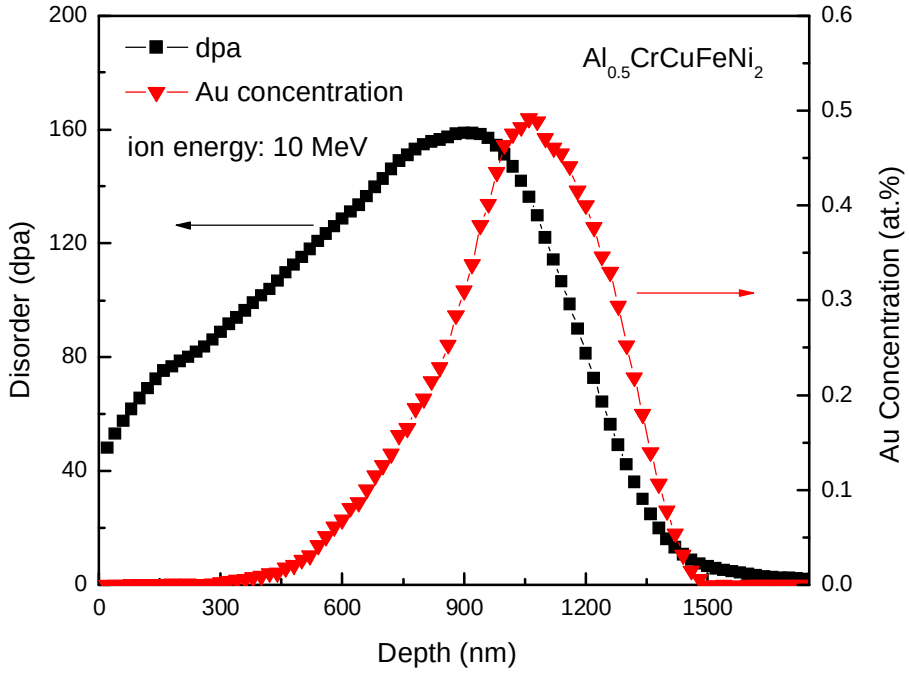

Figure 43 The SRIM-predicted damage profile in the unit of dpa and Au concentration for $Al_{0.5}CrCuFeNi_2$ HEA irradiated by 10 MeV Au to a fluence of 2.0×10^{16} cm^{-2}.

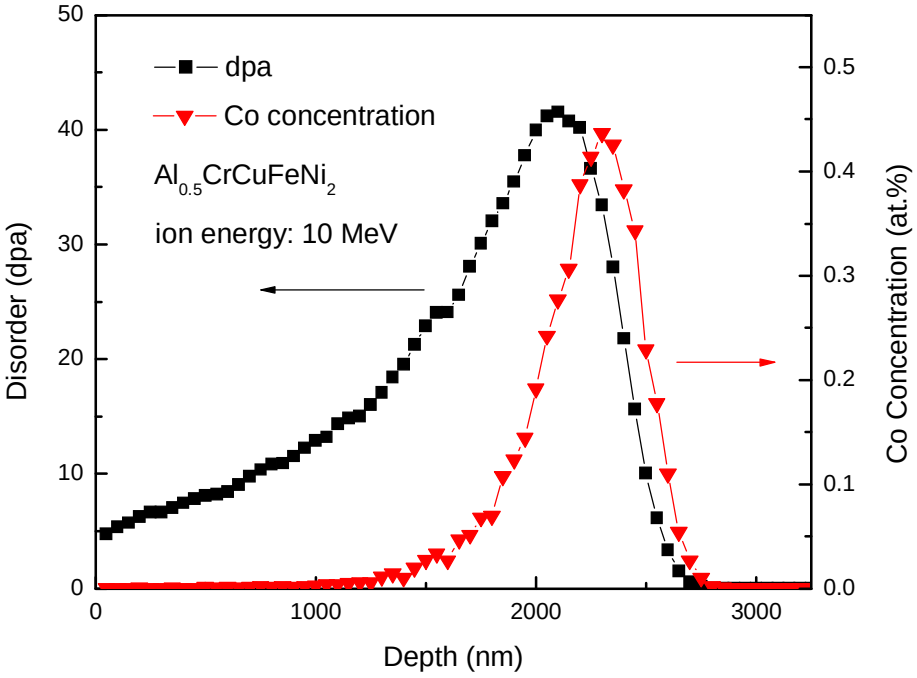

Figure 44 The SRIM-predicted damage profile in the unit of dpa and Co concentration for $Al_{0.5}CrCuFeNi_2$ HEA irradiated by 10 MeV Co to a fluence of 2.0×10^{16} cm^{-2}.

VITA

Yuting Li was born in a small village in Yancheng, Jiangsu Provience, China on September 15, 1983. He received his bachelor's degree in Material Science from Yancheng Institute of Technology in July 2005. He continued his graduate study in Chemistry and Chemical Engineering in Shenzhen University and obtained M.S. in June 2009. In August of 2011, he entered University of Tennessee, Knoxville in Materials Science and Engineering department. He received his Master degree in August of 2013.